



THE BRIDGE

MATERIALS ANALYSIS eNEWSLETTER
JANUARY 2014, ISSUE 7

| | |
|--|----------|
| The ZSX Primus WDXRF Series Flexibility, Sensitivity and Reliability | 2 |
| Customer in the Spotlight D/MAX RAPID II – VariMax CMF with diamond anvil cell in Geodynamics Research Center, Ehime University | 2 |
| Scientific Book Review | 3 |
| Featured Application Note EDXRF analysis of finished Portland cement | 3 |
| Featured Rigaku Journal Article – XRD Detector solutions and those applications for material science X-ray diffractometer (1) | 4 |
| European SmartLab Workshop | 4 |
| Featured Rigaku Journal Article – WDXRF Trace heavy element analysis for wastewater and river water by X-ray fluorescence spectrometry | 5 |
| Rigaku Conferences | 6 |
| Material Analysis in the News | 6 |
| The Adventures of Captain Nano | 7 |
| Recent Scientific Papers of Interest | 8 |

Welcome

It is a new year and so it is time to try something different. We appreciate people who take the time to read our newsletter and feel an obligation to provide useful information that will help them in their work. In this issue we are going to start the serialization of a training textbook that has been developed in Rigaku's application laboratory for the teaching of thin film diffraction analysis. Some academic shared resource facilities now report a 50/50 split in people who are using XRD for powder and those using it to study thin films. We hope that by publishing our thin film training textbook over the next year in our newsletter that people who want to learn about thin film analysis or would like to have a refresher course, will benefit from it.

We particularly encourage you to forward this to any student who might encounter thin film diffraction in the future.

Enjoy the newsletter.

A bridge is often used to symbolize a connection or link between two places, and thus we felt The Bridge would be the perfect name for our eNewsletter, as we hope that it will act as a vehicle for the transmission of ideas and information between Rigaku and interested readers around the world.

And a bridge is a two-way structure, a concept that we will keep in mind as we not only provide information about Rigaku, but also report on interesting research and the associated laboratories around the world, publish technical book reviews that might help our readers in their work, and highlight general news topics that are of interest to many people involved in materials analysis.



Photo by Paul Swebston

Customer in the Spotlight

D/MAX RAPID II – VariMax CMF with diamond anvil cell
in Geodynamics Research Center, Ehime University, Japan

The Geodynamics Research Center (GRC) is an advanced research center of Ehime University and focuses on studying the structure, composition and dynamics of the Earth's deep interior.

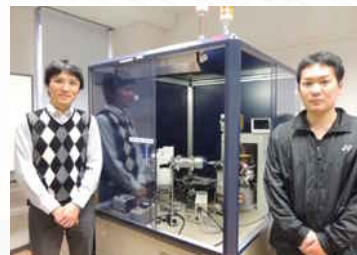
GRC is famous for their research facility, which contains extensive high temperature and high-pressure instrumentation. Their multi-anvil press instruments are named after cultural icons of the Ehime Prefecture and are called "ORANGE", "MADONNA", and "BOTCHAN". This equipment is used to synthesize minerals/rocks that are expected to be present in the Earth's interior and novel hard materials at high pressure (generally up to 25 GPa) and high temperature up to 2,500°C. In addition, Prof. Tetsuo Irifune, President of the GRC, is well known for his synthetic nano-polycrystalline diamond called "HIME-DIA," which is characterized by its ultra-high hardness and superior mechanical properties.

The main objective of high-pressure Earth Science research is to understand the structure and dynamics of the Earth's deep interior through experimental and theoretical studies on the phase transitions and chemical and physical processes of minerals/rocks (chemical compounds) under very high pressure and high temperature.

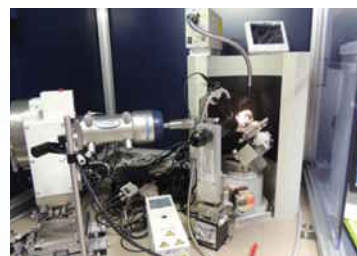
For experimental synthesis of such minerals/rocks, they use large-volume (multi-anvil) presses and diamond anvil cells. For the examination of the recovered products, they employ a variety of analytical facilities such as powder X-ray diffraction (PXRD), RAMAN, SEM-EDS, ATEM, which are all equipped in the research center. PXRD is very useful for phase identification, crystal structure and orientation analysis, etc.

Associate Prof. Hiroaki Ohfuji is in charge of the Rigaku D/MAX RAPID II – CMF at the Ultra High Pressure Laboratory in GRC. He and his colleagues use the D/MAX RAPID II – CMF for identification of the mineral phases in the samples recovered from high pressure experiments and also for *in-situ* measurements of materials under pressure in a diamond anvil cell to study

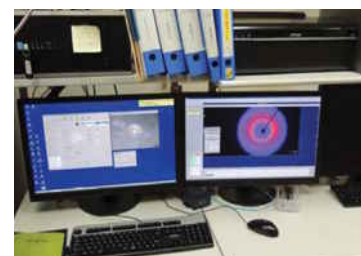
the crystal structure of high-pressure phases and their pressure-volume relation. He also uses the facility for the analysis of lattice preferred orientation of polycrystalline materials based on 2D diffraction data collected with a MoKa beam.



Associate Prof. Ohfuji (left side) and his student



The D/MAX RAPID II - CMF is an X-ray diffractometer with a curved imaging plate (IP) detector, designed specifically for micro-area analyses. It is equipped with a microfocus rotating anode X-ray generator that provides high intensity for micro-area analyses, and side-by-side laterally graded multilayer optics to focus the beam. It can be used for measurements of samples as small as 0.01 mm and also accommodate a diamond anvil cell for *in-situ* measurements under high pressure.



According to associate Prof. Ohfuji, the D/MAX RAPID II-CMF currently has 30~50 users in Ehime University. This instrument is in operation day after day, not only for the GRC staffs and students but also for people from outside for collaborative researchers.

The ZSX® Primus WDXRF Series

Flexibility, Sensitivity
and Reliability

The Rigaku ZSX Primus Series sequential WDXRF spectrometers deliver rapid quantitative determination of major and minor atomic elements, from beryllium through uranium, in the widest possible variety of sample types — with or without standards.

[Click here for more information on Rigaku's ZSX Series spectrometers](#)

Scientific Book Review

Common Errors in Statistics (and How to Avoid Them)

by Phillip I. Good and James W. Hardin

John Wiley and Sons, Inc., 2012, ISBN 978-1-118-29439-0

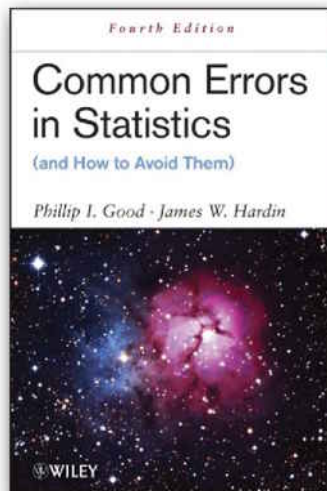
I saw a review of this book in *Scientific Computing* and thought it looked interesting. I did not read the review to avoid any bias, but had I read it, I might not have bought the book. Don't get me wrong: it is very good, and there is much to be learned if you are willing to stop and think as you read it.

The focus of the book is on the application of statistics to the medical field, mostly in the context of the effects of treatments on patients. There are points that may be confusing to a crystallographer. For example, there is a short, funny diatribe on maximum likelihood that, while correct, does not apply to its usage in crystallography, since we generally work with normal distributions. There is also a section on how not to create bogus priors for Bayesian analysis. The scary part is that the judicial system allows falsely generated priors to affect the outcome of civil and criminal cases to no good.

The authors are adamant about designing an experiment such that one can extract the information needed to test the original hypotheses at the end of the trial. They point out the fallacy of stopping studies in the middle or extracting information that was not originally sought because it can introduce a bias. If one sees an unexpected trend, one should go back and design a new trial to properly test the new hypothesis.

Common Errors in Statistics is not an introductory text and requires a basic knowledge of statistics. With each chapter, the authors provide a descriptive "for further reading" list, as well as copious references to enhance the topics covered.

In the first part of the book, "Foundations," the authors cover sources of error, hypotheses, and collecting data. In the second part, "Statistical Analysis," they discuss data quality assessment, estimation, testing hypotheses, strengths and limitations of procedures, reporting results, interpreting and presenting results. The third section, "Building a Model," covers univariate, multivariate and alternate forms of regression,

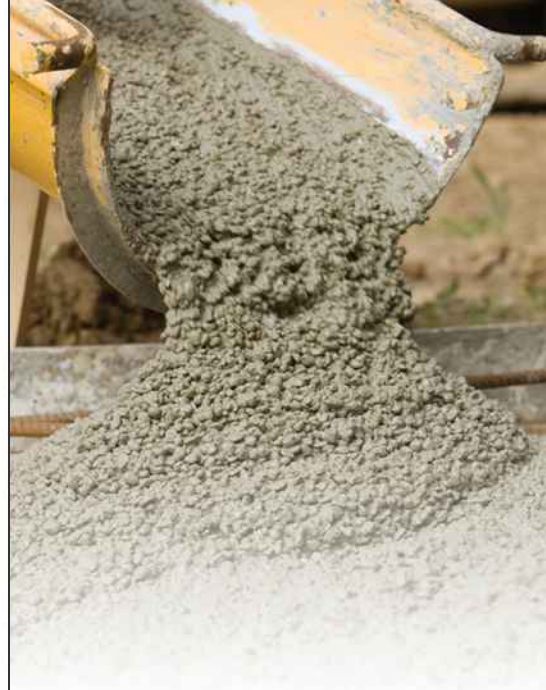


modeling counts and correlated data and validation. The authors discuss data analysis, reporting and presentation and provide useful guidelines for each of these topics.

There are some very funny lines. I won't spoil them all, but one I particularly like is "What is the sound of one hand clapping?" The answer is the same as an experiment without a control. Another bon mot is "a picture is worth 1000 words only if does not take a 1000 words to describe it." That said, there is a very good discussion, a la Tufte, on the display of numerical data and how to draw useful and informative graphs, as well as when to use a table instead of a graph.

As an aside, if you want to read something laugh-out-loud funny, try Dave Barry's *Insane City*. But don't read it on an airplane or your fellow travelers might think you've lost it.

Joseph D. Ferrara, Ph.D.
Chief Science Officer, Rigaku



Featured Application Note

EDXRF analysis of finished Portland cement

EDXRF is a simple analysis technique used in cement plants around the world. The technique is ideal for QA/QC throughout the cement production process. The EDXRF analyzer also makes an excellent backup instrument for the WDXRF analyzer used for final QC and certification.

[Click here to see full application note](#)

• Trend

1 Rigaku's analytical instruments for the production of pharmaceutical grade technologies Pharmaceutical Research

• Technical Articles

4 Drug discovery by single crystal X-ray analysis Pharmaceutical Research

8 Evaluation of polymorphic forms by diffraction and thermal analysis Pharmaceutical Research

10 Pharmaceutical case material: large bandwidth X-ray spectrometry Pharmaceutical Research



Registration deadline: February 14, 2014

Featured Rigaku Journal Article – XRD

Detector solutions and those applications for material science X-ray diffractometer (1)

Shintaro Kobayashi and Katsuhiko Inaba, Application Laboratory, Rigaku Corporation

Dimensional detectors, e.g. 1-D and 2-D, are becoming standard equipment for laboratory based X-ray diffractometers. Rigaku's unique applications using dimensional detectors will be summarized and discussed in the next three newsletters. The first article, featured this month, discusses available detector types and associated application with a focus on 1-D (D/teX Ultra) and 2-D (PILATUS 100K) detectors.

[Click here to see full article](#)

European “SmartLab Applications” Workshop

ANKA – the Synchrotron Radiation Facility at KIT
Thursday, February 27 and Friday, February 28, 2014

Rigaku is organizing a 2-day workshop around the versatile SmartLab® X-ray diffractometer at the ANKA synchrotron. The event will be located at the radiation facility at KIT (Karlsruhe Institute of Technology) and will take place from February 27 – 28, 2014. The workshop will focus on XRD applications and will be dedicated to actual and potential customers: the “SmartLab user family” in Europe. In addition SmartLab users will present state-of-the-art research findings and methods development. We very much look forward to welcoming you to two days of wonderful discussions and fun.



Venue

ANKA Synchrotron Radiation Facility
at KIT (Karlsruhe Institute of Technology)

KIT North Campus
Hermann-von-Helmholtz-Platz 1
76344 Eggenstein-Leopoldshafen,
Germany

Tentative agenda

Thursday, February 27, 2014

13:00 – 17:00

- 13:00 Opening remarks
- 13:10 Corporate presentation
- 13:30 Rigaku XRD solution
- 14:00 Invited speech by a user (1)
- 15:00 Break
- 15:30 Rigaku Software solution: "SmartStudio II"
- 16:30 ANKA beamline tour
- 17:00 Closing
- 19:00 Welcome drink and meal

Friday, February 28, 2014

10:00 – 17:00

- 10:00 Invited speech by a user (2)
- 11:00 What's new on SmartLab
- 12:00 Lunch
- 13:00 Instrument demonstrations on SmartLab
- 14:00 Hints on SmartLab operations
- 15:00 Break
- 15:30 Invited speech by a user (3)
- 16:30 Multilayer and other optics for synchrotron radiation, solutions from EUV to hard X-rays
- 17:00 Closing remarks



Featured Rigaku Journal Article – WDXRF

Trace heavy element analysis for wastewater and river water by X-ray fluorescence spectrometry – Examples for ppm to sub ppm level analysis of heavy elements

*Takao Moriyama,
XRF Application Laboratory,
Rigaku Corporation*

This report introduces an X-ray fluorescence (WDXRF) analysis for the detection of ppb level of a trace of zinc in wastewater and also hazardous heavy elements in river water using a high sensitivity micro-drop-let filter paper, "UltraCarry", and the newly developed vacuum dryer, "UltraDry".

[Click here to see full article](#)

Certificate

Please contact the person listed below if you need an attendance certificate for the workshop.

VISA

Please contact the person listed below if you need an invitation letter for your visa.

Hotel accommodation

Applicants who require hotel accommodation are kindly requested to mention it when applying for the workshop.

Registration

Registration deadline is **Friday, February 14, 2014**.

Registration for the meeting is free of charge and includes a workshop dinner and refreshments. Please register by sending an e-mail to following contact person:

Katja Bechmann (*Sales Administrative, Rigaku Europe SE*)
katja.bechmann@rigaku.com

Questions?

Should you have any questions, please contact the following person by e-mail:

Keisuke Saito (*Marketing Manager XRD, Rigaku Europe SE*)
keisuke.saito@rigaku.com

Material Analysis in the News

News for January 2014

January 6, 2014. From a new element in the periodic table to tremendous advances in the use of graphene, chemists and materials scientists were making breakthroughs in the fields of chemistry and materials science all last year. [Here are some of the most important breakthroughs.](#)

January 7, 2014. The [point spread function of grazing incidence X-ray mirrors](#) can be found using a new self-consistent and flexible computation. The method is based on the Huygens-Fresnel principle (for wave propagation analysis), and it computes the electric field that is diffracted by the 'real' mirror profile to the focal plane.

January 13, 2014. Synchrotron radiation [X-ray fluorescence \(SR-XRF\) analysis reports of a poisoning case by arsenic.](#) In these forensic analyses, SPring-8 and KEK-PF beamlines were used for minor element (Sn, Sb, Mo, Bi, Ba) analysis in the arsenic pesticide specimens, sampled at the crime scene as well as the neighborhood of the suspect.

January 17, 2014. A special issue of the *Journal of X-ray Spectrometry* examines how complementary [X-ray spectrometry methods may assist the forensic investigations](#) of the future. It is evident from this edition that X-ray spectrometry techniques have a great range of potential and exciting new applications, which could have a significant impact on police investigations.

January 20, 2014. Multitalented [graphene is wowing scientists](#) the world over. The *Sydney Morning Herald* reports on those at the forefront of game-changing Australian research.

January 21, 2014. The United Nations has announced that [2014 is the International Year of Crystallography.](#) An opening ceremony, hosted by the United Nations Educational, Scientific and Cultural Organisation (UNESCO) in Paris on 20 January, was followed by a two-day symposium celebrating the technique.

January 21, 2014. A team of researchers from the ESRF, Grenoble, France, and the London Centre for Nanotechnology (LCN) describes the results of their theoretical study of the extent to which it is possible to extract information on the [wave function of complex oxides using resonant X-ray techniques.](#)

January 21, 2014. Gamma valerolactone, the [secret sauce of the new biofuel process.](#) Researchers from the University of Wisconsin – Madison have figured out a chemical treatment that, given a bit of time, can completely dissolve any plant matter, including wood.

January 21, 2014. [Projecting on transparent screens](#) is possible, thanks to specially designed nanoparticles. Researchers at the Massachusetts Institute of Technology have come up with a method that they say is cheaper than current methods, using nanoparticles that interact with a single color in the visible spectrum.

January 21, 2014. Water ice is the most abundant solid material in the universe. Much of it was created as the byproduct of star formation, but not all of it. John Bradley of Lawrence Livermore National Laboratory and his team may have discovered a new source of water in our solar system. His lab experiments reveal that the [solar wind may be creating water on interplanetary dust.](#)

January 21, 2014. The National Association of Colleges and Employers (NACE), the non-profit group that puts together the salary information, has released a table showing the starting [salary breakdown for the 10 top-earning specialized degrees.](#) It turns out that grads who majored in petroleum engineering earn, on average, \$32,500 a year more than mechanical engineering majors.



Conferences

Rigaku exhibited (photo above) at the MRS Fall Meeting Dec. 1 – 6 in Boston, MA, USA. In total, 5,773 papers in 52 scientific sessions were submitted to the material research society (MRS) during the conference.

Rigaku will be sponsoring, attending or exhibiting at the following conferences and trade shows:

Southern African Powder Diffraction Conference and Workshop

Johannesburg, South Africa
January 27 – 31

Biophysical Symposium

San Francisco, CA, USA
February 15 – 19

[Click here to see the complete list](#)

The Adventures of Captain Nano

MOVIN' — Nano-scaled, the Captain sets out to confront the NIBs once more. This time he's got wheels.

Captain Nano - Movin'



Baoxing Xu and Xi Chen* suggested spinning the water molecule in this C60 fullerene should cause its fullerene shell to move in the spin direction. Let me add a little electronic charge to get the molecule spinning and...will you look at that.

*Baoxing Xu and Xi Chen - Electric-Driven Transport of Endohedral Fullerene Encapsulating a Single Water Molecule (2013) PRL, 110, 156103 (2013)



© 20140111 Adam Courville

Recent Scientific Papers of Interest

Irradiation effects and micro-structural changes in large grain uranium dioxide fuel investigated by micro-beam X-ray diffraction.

Mieszczynski, C.; Kuri, G.; Deguelde, C.; Martin, M.; Bertsch, J.; Borca, C.N.; Grolimund, D.; Delafoy, Ch.; Simoni, E. *Journal of Nuclear Materials*. Jan2014, Vol. 444 Issue 1-3, p274-282. 9p.
[DOI: 10.1016/j.jnucmat.2013.09.054](https://doi.org/10.1016/j.jnucmat.2013.09.054).

Characterization of iron in airborne particulate matter.

Tavares, F. V. F.; Ardisson, J. D.; Rodrigues, P. C. H.; Brito, W.; Macedo, W. A. A.; Jacomino, V. M. F. *Hyperfine Interactions*. Jan2014, Vol. 224 Issue 1-3, p109-119. 11p.
[DOI: 10.1007/s10751-013-0823-8](https://doi.org/10.1007/s10751-013-0823-8).

Chemical composition of marine sediments in the Pacific Ocean from Sinaloa to Jalisco, Mexico.

Martinez, T.; Tejada, S.; Lartigue, J.; Zarazua, G.; Avila-Perez, P.; Ramos, A.; Navarrete, M.; Muller, G. *Journal of Radioanalytical & Nuclear Chemistry*. Jan2014, Vol. 299 Issue 1, p827-834. 8p.
[DOI: 10.1007/s10967-013-2704-7](https://doi.org/10.1007/s10967-013-2704-7).

Characterization of lead glazed potteries from Smyrna (Izmir/Turkey) using multiple analytical techniques; Part II: Body.

Özçatal, M.; Yaygingöl, M.; Issi, A.; Kara, A.; Turan, S.; Okyar, F.; Pfeiffer Taş, Ş.; Nastova, I.; Grupče, O.; Minčeva-Šukarova, B. *Ceramics International*. Jan2014, Vol. 40 Issue 1, p2153-2160. 8p.
[DOI: 10.1016/j.ceramint.2013.07.132](https://doi.org/10.1016/j.ceramint.2013.07.132).

Characterization of biomass and high carbon content coal ash for productive reuse applications.

Yeboah, N.N. Nortey; Shearer, Christopher R.; Burns, Susan E.; Kurtis, Kimberly E. *Fuel*. Jan2014, Vol. 116, p438-447. 10p.
[DOI: 10.1016/j.fuel.2013.08.030](https://doi.org/10.1016/j.fuel.2013.08.030).

Structural and elemental X-ray microanalysis with synchrotron radiation in confocal geometry.

Sosa, Carlos M.; Sánchez, H. Jorge; Pérez, Carlos A.; Perez, Roberto D. *Nuclear Instruments & Methods in Physics Research Section B*. Jan2014, Vol. 319, p171-176. 6p.
[DOI: 10.1016/j.nimb.2013.10.021](https://doi.org/10.1016/j.nimb.2013.10.021).

Simultaneous assessment of phase chemistry, phase abundance and bulk chemistry with statistical electron probe micro-analyses: Application to cement clinkers.

Wilson, William; Krakowiak, Konrad J.; Ulm, Franz-Josef. *Cement & Concrete Research*. Jan2014, Vol. 55, p35-48. 14p.
[DOI: 10.1016/j.cemconres.2013.09.013](https://doi.org/10.1016/j.cemconres.2013.09.013).

Measurements of liquid and glass structures using aerodynamic levitation and in-situ high energy x-ray and neutron scattering.

Weber, J.K.R.; Benmore, C.J.; Skinner, L.B.; Neuefeind, J.; Tumber, S.K.; Jennings, G.; Santodonato, L.J.; Jin, D.; Du, J.; Parise, J.B. *Journal of Non-Crystalline Solids*. Jan2014, Vol. 383, p49-51. 3p.
[DOI: 10.1016/j.jnoncrysol.2013.03.035](https://doi.org/10.1016/j.jnoncrysol.2013.03.035).

Structure analysis and multiferroic properties of Zr⁴⁺ doped BiFeO₃ ceramics.

Xie, Junjie; Feng, Chude; Pan, XiuHong; Liu, Yan. *Ceramics International*. Jan2014, Vol. 40 Issue 1 Part A, p703-706. 4p.
[DOI: 10.1016/j.ceramint.2013.06.058](https://doi.org/10.1016/j.ceramint.2013.06.058).

Study of crystallization of PbO-WO₃-P₂O₅ glasses by thermoanalytical and spectroscopic methods.

Rösslerová, Ivana; Koudelka, Ladislav; Černošek, Zdeněk; Mošner, Petr; Beneš, Ludvík. *Journal of Non-Crystalline Solids*. Jan2014, Vol. 384, p41-46. 6p.
[DOI: 10.1016/j.jnoncrysol.2013.05.006](https://doi.org/10.1016/j.jnoncrysol.2013.05.006).

Mössbauer and X-ray study of the Fe₆₅Ni₃₅ invar alloy obtained by mechanical alloying.

Rodriguez, R. R.; Valenzuela, J. L.; Tabares, J. A.; Pérez Alcázar, G. A. *Hyperfine Interactions*. Jan2014, Vol. 224 Issue 1-3, p323-330. 8p.
[DOI: 10.1007/s10751-013-0834-5](https://doi.org/10.1007/s10751-013-0834-5).

Study of titanate nanotubes by X-ray and electron diffraction and electron microscopy.

Brunatova, Tereza; Popelkova, Daniela; Wan, Wei; Oleynikov, Peter; Danis, Stanislav; Zou, Xiaodong; Kuzel, Radomir. *Materials Characterization*. Jan2014, Vol. 87, p166-171. 6p.
[DOI: 10.1016/j.matchar.2013.11.010](https://doi.org/10.1016/j.matchar.2013.11.010).

Quasi-monoenergetic and tunable X-rays from a laser-driven Compton light source.

Powers, N. D.; Ghebregziabher, I.; Golovin, G.; Liu, C.; Chen, S.; Banerjee, S.; Zhang, J.; Umstadter, D. P. *Nature Photonics*. Jan2014, Vol. 8 Issue 1, p28-31. 4p.
[DOI: 10.1038/nphoton.2013.314](https://doi.org/10.1038/nphoton.2013.314).

Neutron scattering—The key characterization tool for nanostructured magnetic materials.

Fitzsimmons, M.R.; Schuller, Ivan K. *Journal of Magnetism & Magnetic Materials*. Jan2014, Vol. 350, p199-208. 10p.
[DOI: 10.1016/j.jmmm.2013.09.028](https://doi.org/10.1016/j.jmmm.2013.09.028).

Temperature dependence of molecular dynamic arrangement in the vicinity of the glass transition of MEH-PPV: C60 based structures: X ray and impedance spectroscopy analysis.

Dhibi, O.; Ltaief, A.; Zghal, S.; Bouazizi, A. *Vacuum*. Jan2014, Vol. 99, p80-88. 9p.
[DOI: 10.1016/j.vacuum.2013.03.021](https://doi.org/10.1016/j.vacuum.2013.03.021).

Spatially Resolved In Situ Measurements of the Ion Distribution Near the Surface of Electrode in a Steady-State Diffusion in an Electrolytic Tank with Confocal Micro X-ray Fluorescence.

Song Peng; Zhiguo Liu; Tianxi Sun; Yongzhong Ma; Xunliang Ding. *Analytical Chemistry*. 1/7/2014, Vol. 86 Issue 1, p362-366. 5p.
[DOI: 10.1021/ac403188k](https://doi.org/10.1021/ac403188k).

Rapid, Nondestructive Elemental Analysis of Tree and Shrub Litter.

Tighe, Matthew; Forster, Nicola. *Communications in Soil Science & Plant Analysis*. Jan2014, Vol. 45 Issue 1, p53-60. 8p.
[DOI: 10.1080/00103624.2013.848878](https://doi.org/10.1080/00103624.2013.848878).

Correlation between the residual stress and the density of threading dislocations in GaN layers grown by hydride vapor phase epitaxy.

Barchuk, M.; Röder, C.; Shashev, Y.; Lukin, G.; Motylenko, M.; Kortus, J.; Pätzold, O.; Rafaja, D. *Journal of Crystal Growth*. Jan2014, Vol. 386, p1-8. 8p.
[DOI: 10.1016/j.jcrysgro.2013.09.041](https://doi.org/10.1016/j.jcrysgro.2013.09.041).

Conversion of aluminum foil to powders that react and burn with water.

Narayana Swamy, Ashvin Kumar; Shafirovich, Evgeny. *Combustion & Flame*. Jan2014, Vol. 161 Issue 1, p322-331. 10p.
[DOI: 10.1016/j.combustflame.2013.08.017](https://doi.org/10.1016/j.combustflame.2013.08.017).

Lattice deformation of wurtzite Mg_xZn_{1-x}O alloys: An extended X-ray absorption fine structure study.

Zheng, Wei; Feng, Zhe Chuan; Lee, Jyh-Fu; Wu, Dong-Sing; Zheng, Rui Sheng. *Journal of Alloys & Compounds*. Jan2014, Vol. 582, p157-160. 4p.
[DOI: 10.1016/j.jallcom.2013.08.021](https://doi.org/10.1016/j.jallcom.2013.08.021).

In Situ Observation of Cu-Ni Alloy Nanoparticle Formation by X-Ray Diffraction, X-Ray Absorption Spectroscopy, and Transmission Electron Microscopy: Influence of Cu/Ni Ratio.

Wu, Qiongxiao; Duchstein, Linus D. L.; Chiarello, Gian Luca; Christensen, Jakob M.; Damsgaard, Christian D.; Elkjær, Christian F.; Wagner, Jakob B.; Temel, Burcin; Grunwaldt, Jan-Dierk; Jensen, Anker D. *ChemCatChem*. Jan2014, Vol. 6 Issue 1, p301-310. 10p.
[DOI: 10.1002/cctc.201300628](https://doi.org/10.1002/cctc.201300628).

Analysis of the elemental composition of Tang Sancai from the four major kilns in China using EDXRF.

Ma, Bo; Liu, Long; Feng, Song-Lin; Xu, Qing; Feng, Xiang-Qian. *Nuclear Instruments & Methods in Physics Research Section B*. Jan2014, Vol. 319, p95-99. 5p.
[DOI: 10.1016/j.nimb.2013.11.011](https://doi.org/10.1016/j.nimb.2013.11.011).

Critical Exponents for Solvent Extraction Resolved Using SAXS.

Ross J. Ellis. *Journal of Physical Chemistry B*. Jan2014, Vol. 118 Issue 1, p315-322. 8p.
[DOI: 10.1021/jp408078v](https://doi.org/10.1021/jp408078v).

XRD and Raman study on crystal structures and dielectric properties of Ba[Mg_{(1-x)/3}Zr_xNb_{2(1-x)/3}]O₃ solid solutions.

Zhang, Han; Diao, Chuanling; Liu, Shulian; Jiang, Shouzheng; Jing, Xiping; Shi, Feng. *Ceramics International*. Jan2014, Vol. 40 Issue 1, p2427-2434. 8p.
[DOI: 10.1016/j.ceramint.2013.08.016](https://doi.org/10.1016/j.ceramint.2013.08.016).

On the crystallinity of PVA/palm leaf bio-composite using DSC and XRD techniques.

Patel, Arunendra; Bajpai, R.; Keller, J. *Microsystem Technologies*. Jan2014, Vol. 20 Issue 1, p41-49. 9p.
[DOI: 10.1007/s00542-013-1882-0](https://doi.org/10.1007/s00542-013-1882-0).

Ten seconds in the field: rapid Armenian obsidian sourcing with portable XRF to inform excavations and surveys.

Frahm, Ellery; Schmidt, Beverly A.; Gasparyan, Boris; Yeritsyan, Benik; Karapetian, Sergei; Meliksetian, Khachatur; Adler, Daniel S. *Journal of Archaeological Science*. Jan2014, Vol. 41, p333-348. 16p.
[DOI: 10.1016/j.jas.2013.08.012](https://doi.org/10.1016/j.jas.2013.08.012).

PIXE and XRF analysis of atmospheric aerosols from a site in the West area of Mexico City.

Díaz, R.V.; López-Monroy, J.; Miranda, J.; Espinosa, A.A. Nuclear Instruments & Methods in Physics Research Section B. Jan2014, Vol. 318 Issue Part A, p135-138. 4p.

[DOI: 10.1016/j.nimb.2013.05.095.](https://doi.org/10.1016/j.nimb.2013.05.095)

Structural investigations in helium charged titanium films using grazing incidence XRD and EXAFS spectroscopy.

Wan, Chubin; Zhou, Xiaosong; Wang, Yuting; Li, Shina; Ju, Xin; Peng, Shuming. Journal of Nuclear Materials. Jan2014, Vol. 444 Issue 1-3, p142-146. 5p.

[DOI: 10.1016/j.jnucmat.2013.09.049.](https://doi.org/10.1016/j.jnucmat.2013.09.049)

Understanding changes in cellulose crystalline structure of lignocellulosic biomass during ionic liquid pretreatment by XRD.

Zhang, Jiafu; Wang, Yixun; Zhang, Liye; Zhang, Ruihong; Liu, Guangqing; Cheng, Gang. Biore-source Technology. Jan2014, Vol. 151, p402-405. 4p. [DOI: 10.1016/j.biortech.2013.10.009.](https://doi.org/10.1016/j.biortech.2013.10.009)

Microstructure of natural graphite flakes revealed by oxidation: Limitations of XRD and Raman techniques for crystallinity estimates.

Badenhorst, Heinrich. Carbon. Jan2014, Vol. 66, p674-690. 17p. [DOI: 10.1016/j.carbon.2013.09.065.](https://doi.org/10.1016/j.carbon.2013.09.065)

XRD analysis and magnetic properties of nanocrystalline Ni₂₀Co₈₀ alloys.

Bensebaa, N.; Loudjani, N.; Alleg, S.; Dekhil, L.; Suñol, J.J.; Al Sae, M.; Bououdina, M. Journal of Magnetism & Magnetic Materials. Jan2014, Vol. 349, p51-56. 6p.

[DOI: 10.1016/j.jmmm.2013.08.045.](https://doi.org/10.1016/j.jmmm.2013.08.045)

XAS and XRD *in situ* characterisation of reduction and reoxidation processes of iron corrosion products involved in atmospheric corrosion.

Monnier, Judith; Réguer, Solenn; Foy, Eddy; Testemale, Denis; Mirambet, François; Saheb, Mandana; Dillmann, Philippe; Guillot, Ivan. Corrosion Science. Jan2014, Vol. 78, p293-303. 11p. [DOI: 10.1016/j.corsci.2013.10.012.](https://doi.org/10.1016/j.corsci.2013.10.012)

SCOPE

The analysis of finished Portland cement is demonstrated using the empirical approach.

BACKGROUND

EDXRF is a simple analysis technique used in cement plants around the world. The technique is ideal for QA/QC throughout the cement production process. EDXRF can be used as a screening tool and a quality control analyzer to ensure proper composition of incoming feedstocks, raw meal mixture balances, addition of gypsum and throughout the manufacturing process. The EDXRF analyzer also makes an excellent backup instrument for the WDXRF analyzer used for final QC and certification.



INSTRUMENTATION

- Model:** Rigaku NEX CG
- X-ray tube:** 50 W Pd-anode
- Targets:** Standard Targets plus
Light Element Target Option
- Detector:** SDD
- Sample Type:** Hydraulically-pressed pellets
- Analysis Time:** 1200 seconds
- Environment:** Helium Purge
- Standard:** 15-position Sample Tray (32mm)
- Optional:** 10-position Sample Tray (40mm)



SAMPLE PREPARATION

Each sample is prepared by grinding to a fine, dry, homogeneous powder of <200 mesh (<75um particle size) using a ball mill or ring-and-puck shatterbox. For measurement, a sample is prepared by weighing 5 grams of sample and making a hydraulically pressed pellet using 20 tons pressure for 30 seconds.

CALIBRATION

Empirical calibrations were built using a set of 8 NIST SRM certified standards: 1880b, 1881a, 1884b, 1885a, 1886a, 1887a, 1888a, 1889a. Using the empirical approach, "alpha corrections" are then employed to automatically compensate for variations in X-ray absorption and enhancement effects within the sample due to the independent variations in element concentration, thus yielding a very accurate model characterizing the cement type. A separate calibration method should be setup for Raw Meal, Clinker and Finished cements. A summary of the finished Portland cement empirical calibration is shown here.

| Component | Concentration Range (mass%) | RMS Deviation | R ² Confidence |
|--------------------------------|-----------------------------|---------------|---------------------------|
| SiO ₂ | 18.637 – 22.380 | 0.057 | 0.9992 |
| Al ₂ O ₃ | 3.875 – 7.060 | 0.083 | 0.9979 |
| Fe ₂ O ₃ | 0.152 – 3.681 | 0.036 | 0.9995 |
| CaO | 57.58 – 67.87 | 0.16 | 0.9989 |
| MgO | 0.814 – 4.740 | 0.082 | 0.9984 |
| SO ₃ | 2.086 – 4.622 | 0.062 | 0.9980 |
| Na ₂ O | 0.091 – 1.068 | 0.019 | 0.9986 |
| K ₂ O | 0.093 – 1.228 | 0.023 | 0.9987 |
| TiO ₂ | 0.0840 – 0.3706 | 0.0055 | 0.9979 |
| P ₂ O ₅ | 0.0220 – 0.3060 | 0.0094 | 0.9955 |
| ZnO | 0.0010 – 0.1070 | 0.0005 | 0.9999 |
| Mn ₂ O ₃ | 0.0073 – 0.2588 | 0.0034 | 0.9992 |
| Cl | 0.0019 – 0.0183 | 0.0011 | 0.9825 |
| SrO | 0.0180 – 0.6380 | 0.0019 | 0.9999 |

REPEATABILITY

To demonstrate repeatability (precision), NIST SRM 1887a was chosen from the set of calibration standards. The sample was measured in static position for ten repeat analyses using a total analysis time of 1200 sec per measurement, with typical results shown below.

| NIST SRM 1887a | SiO ₂ | Al ₂ O ₃ | Fe ₂ O ₃ | CaO | MgO | SO ₃ | Na ₂ O | K ₂ O | TiO ₂ | P ₂ O ₅ | ZnO | Mn ₂ O ₃ | Cl | SrO |
|--------------------|------------------|--------------------------------|--------------------------------|-------|------|-----------------|-------------------|------------------|------------------|-------------------------------|-------|--------------------------------|--------|-------|
| Standard Value | 18.64 | 6.20 | 2.86 | 60.90 | 2.84 | 4.62 | 0.478 | 1.10 | 0.266 | 0.306 | 0.067 | 0.119 | 0.0104 | 0.322 |
| Average Value | 18.68 | 6.13 | 2.83 | 61.15 | 2.75 | 4.62 | 0.465 | 1.12 | 0.256 | 0.304 | 0.067 | 0.116 | 0.0112 | 0.323 |
| Standard Deviation | 0.05 | 0.02 | 0.01 | 0.10 | 0.03 | 0.02 | 0.016 | 0.01 | 0.002 | 0.002 | 0.001 | 0.001 | 0.0001 | 0.001 |

Reducing the analysis time to 600 sec results in an increase in each standard deviation by a factor of 1.4.

TYPICAL DETECTION LIMITS

To determine the Lower Limit of Detection (LLD) using the empirical method, ten repeat analyses of a sample pellet of CaO was measured and the standard deviation calculated. CaO represents a high calcium "blank" cement matrix. The LLD is then defined as three times the standard deviation. This approach ensures that analyses above the determined LLD are measuring signal above background in a cement matrix. The following LLDs were determined using the same analysis times employed for calibration and repeatability. Actual detection limits may vary based on analysis time used, combinations of elements present and elemental concentration levels.

| Component | LLD (mass%) |
|--------------------------------|-------------|
| SiO ₂ | 0.0030 |
| Al ₂ O ₃ | 0.0036 |
| Fe ₂ O ₃ | 0.0006 |
| MgO | 0.020 |
| SO ₃ | 0.0003 |
| Na ₂ O | 0.062 |
| K ₂ O | 0.012 |
| TiO ₂ | 0.0021 |
| P ₂ O ₅ | 0.0006 |
| ZnO | 0.0001 |
| Mn ₂ O ₃ | 0.0003 |
| Cl | 0.0002 |
| SrO | 0.0003 |

The LLDs shown here represent real life detection limits in a matrix containing very high calcium using an analysis time of 1200 sec. Reducing the analysis time to 600 sec results in an increase in each LLD by a factor of 1.4

CONCLUSION

The Rigaku NEX CG combines indirect excitation with secondary targets, polarization targets and a high performance SDD detector to yield the optimum performance for elemental analysis of cement. During the entire production and processing cycle, oxide composition of the cement material must be reliably monitored to ensure optimal process control, physical characteristics of the cement, as well as profitability. The Rigaku NEX CG analyzer is an ideal tool throughout the quality control process and as a backup to WDXRF systems. In addition, the NEX CG is demonstrated to meet ASTM C114 testing criteria, with performance shown in Application Note #1027, making the NEX CG a versatile and valuable tool for several applications within the cement industry.

X-ray thin-film measurement techniques

VIII. Detectors and series summary

Shintaro Kobayashi* and Katsuhiko Inaba*

1. Introduction

The various XRD techniques as the characterization tools for thin film samples have been presented in this series of “X-ray thin-film measurement technique” lecture course. There has heretofore been remarkable progress with detectors equipped with XRD apparatus. In this lecture, some explanation of the features and functions of 1-dimensional (1D)/2-dimensional (2D) detectors should be presented before summarizing this technical lecture course.

2. Detectors for XRD system

As has been shown in first lecture of the series⁽¹⁾, an X-ray diffractometer system for thin film characterization is composed of 5 parts:

1. X-ray source
2. Incident optical system
3. Goniometer
4. Receiving optical system
5. Detection section

Scintillation counters and proportional counters are the most popular detectors for XRD systems and they are regarded as 0-dimensional (0D) detectors (or point detectors) because they do not have position information on the surface of the detecting components. Recently, however, detectors equipped with many detector-elements on its detection area have also come into general use in laboratory equipment. They are referred to as 1D or 2D detectors used for the high speed measurement. The functions and features of these detectors can be seen in references (2)~(5).

The variation of typical detectors available with the SmartLab system is shown in Fig. 1.

2.1. 0D Detector

The scintillation counter (SC) is mainly used for the SmartLab system because of its good sensitivity, low noise level and easy handling, etc. This detector can measure the count-rate from 0.1 to several 100,000 counts/second after the counting-loss correction.

Using SC, diffracted signals from a sample are

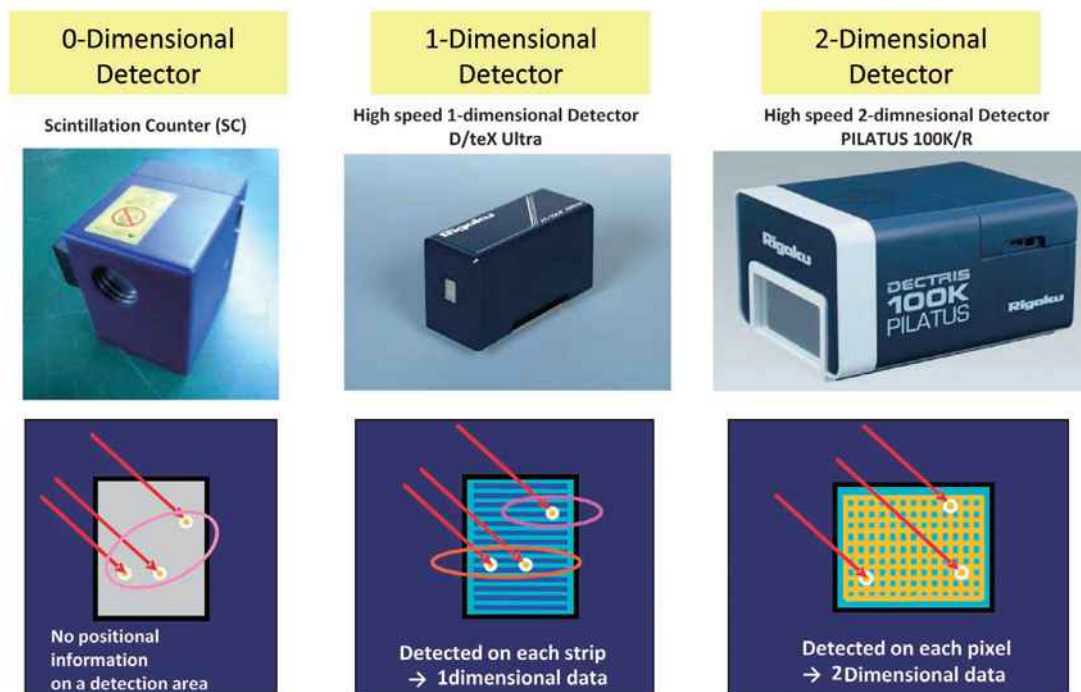


Fig. 1. Typical detectors for SmartLab system.

* Application Laboratories, Rigaku Corporation.

detected with wide detection area of a diameter around 1 inch. This type of detector, known as a 0D detector, does not have positional sensitivity, thus the signals for a given range of 2θ angles are summed up. In order to attain the angle resolution for 2θ , suitable receiving optics should be installed in front of the 0D detector, such as single or double receiving slits or a parallel slit analyzer (PSA), etc.

The wide detection area of SC is utilized by a PSA as a receiving element. By using PSA, it becomes possible to collect the signals spread and scattered on a sample surface without losing the angular resolution. In this lecture series, this situation was explained in the lectures on “Thin-film XRD method” in the 2nd lecture⁽⁶⁾ and “In-plane XRD method” in the 4th lecture⁽⁷⁾.

2.2. 1D Detector

It is getting easier to obtain solid-state semiconductor devices for X-ray detectors. By using this semiconductor device, detecting elements in a shape of strips are arranged in a one-dimensional array with narrow intervals. In recent years, this kind of solid-state semiconductor device has come to be utilized for the X-ray detector in a conventional X-ray diffractometer, and is usually referred to as a “high-speed 1D detector”. This detector is imbued with characteristics of high response and high energy discrimination, but the high speed measurement with this detector is actually enabled by the arranged strips on the detection area.

2.2.1. Principle of performing “high-speed measurement”

Figure 2 shows a measuring geometry for the Bragg-Brentano (BB) para-focusing method. Figure 2(a) shows a typical geometry for the measurement with a 0D detector (SC). The angle resolution is controlled by the combination of incident and receiving slits. Usually, narrow slits around 0.1 mm to 0.5 mm are employed for receiving slits, and this means, only a few parts of detection area of SC are utilized for this measurement. On the other hand, Figure 2(b) shows geometry of the BB method using a 1D detector (D/teX Ultra). In this geometry, narrow receiving slits which are employed in measurements with a 0D detector will be no longer used, but diffracted signals for different 2θ angles can be detected by strips on the detection area simultaneously. In the case of $\theta/2\theta$ scan, the intensity is integrated by a

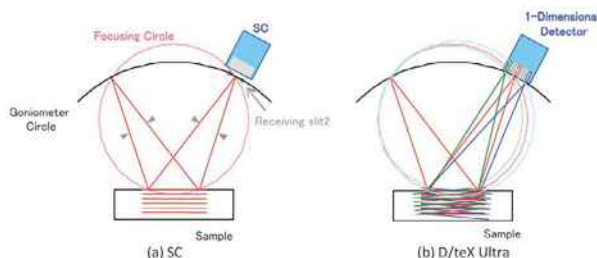


Fig. 2. Geometry of SC (0-dimensional detector) and 1-dimensional detector.

number of strips. This mode is referred to as “Time Delay Integration (TDI)” mode measurement. This is how “high-speed measurement” is enabled^{(8),(9)}.

This technique is effective for measurements by the para-focusing method for samples with textures of random orientation. For a sample with a texture of strong preferred orientation measured with a Parallel Beam (PB) geometry, this advantage of signal integration will be greatly reduced.

Signal integration cannot be restricted to the diffracted signals, but also is adapted inevitably to the signals of X-ray fluorescence from samples, which causes high background noises. For the solution of this problem, Rigaku’s 1D detector, “D/teX Ultra”, is equipped with a function called fluorescence-reduction mode. In this mode of measurement, the range of energy levels for signal integration can be controlled utilizing the energy discrimination of the semiconductor detector^{(2),(9)}.

2.2.2. 1D detector for thin film samples

Some notes and features using a 1D detector for a thin film sample are listed below.

- Conventional $2\theta/\omega$ measurement

As explained in the previous section, the advantage of signal integration (thus high-speed measurements) will be greatly reduced for samples with a texture of strong preferred orientation measured with a Parallel Beam (PB) geometry. If the divergence of the incident X-ray is larger, the integration effect increases. Angular resolution nevertheless, will be decreased.

By using this detector however, weak signals can be detected in a short time, which is advantageous for samples of small amount or minor phase detection⁽⁹⁾, and also for the analysis of phase transitions in samples in a short time⁽⁸⁾.

- Reciprocal space map measurement

A 1D detector has an advantage in Reciprocal Space Map (RSM) measurement in the field of high resolution thin film sample measurement. RSMs using conventional scintillation counters, are measured by the iterative motion of ω -step motions and $2\theta/\omega$ scans by changing scattering vector direction⁽¹⁰⁾. This measuring sequence cannot be directly applied to 1D detection. This is because a 1D detector in the TDI mode will integrate the scattering vector of different directions in the course of $2\theta/\omega$ scan. Instead, this problem will be cleared by iterative motion of ω -step and 2θ scans in TDI mode (not with $2\theta/\omega$ scan), and then, 2-dimensional RSM data can be obtained (Fig. 3). This measuring sequence with TDI mode is useful for RSM where data of a wide range of 2θ will be measured. Since the strip arrangement of detecting elements can cover a certain range of 2θ without scanning of 2θ (i.e., the detector is standing still), signals for a certain range of 2θ can be simultaneously collected by exposing an incident X-ray (with a fixed ω) for a short time. This mode of signal collection is called “Still mode” measurement (Fig. 4), and then, a high-speed

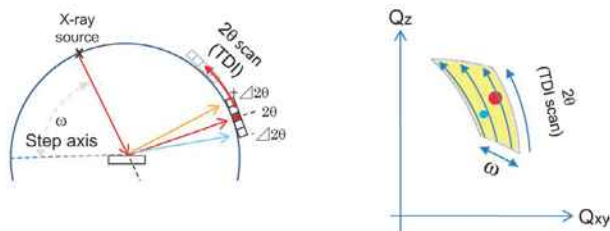


Fig. 3. Reciprocal Space map measurement by D/teX Ultra (ω step and 2θ scan) Left: Schematic illustration of goniometer movement, Right: Diagram of scanned area in reciprocal space.

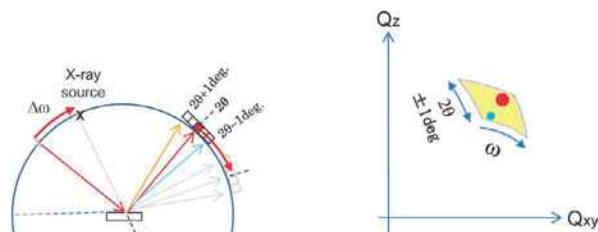


Fig. 4. Reciprocal Space map measurement by D/teX Ultra (2θ step and ω scan) Left: Schematic illustration of goniometer movement, Right: Diagram of scanned area in reciprocal space.

measurement is attained, due to the multiplication of the number of strips of detecting elements. In the SmartLab system, the two measurement modes above are installed.

Figure 3 shows ω -step 2θ -scan measurement for reciprocal space mapping using 1D detector. An ω angle is fixed for every step while 2θ scan. This method has an advantage for wide angle measurement.

Figure 4 shows 2θ -step ω -scan measurement for reciprocal space mapping using 1D detector. By this method, 2θ angle will be fixed while ω axis scanning. This method has advantage for small angle ($\Delta 2\theta < 2^\circ$) measurement. This scanning mode is not a TDI mode, so the intensity will not be integrated. Instead of integration, scattering vector of different angle can be obtained simultaneously. And by scanning of ω axis, reciprocal space map can be obtained. This method is also an advantage of 1D detector.

For the RSM measurement, the geometry of incident/diffracted X-ray is also important. Figures 5 (a) and (b) show 2 different geometries for asymmetric RSM measurements. In general, low incident angle geometry (also called as Grazing-Incident geometry) is convenient for detecting weak signals from thin films. Thus, the geometry shown in Fig. 5(a) is generally employed for measurements for thin film samples, but the incident beam is spread over the sample surface due to the low incident angle, and consequently, the width of diffracted beam is wide.

Another geometry, i.e., low exit angle geometry (also called as Grazing-Exit geometry) is possible to be employed for measuring thin film samples (Fig. 5(b)), where a width of diffracted X-ray beam will be narrower than the one for the incident beam. For the RSM measurements using a 1D detector, the width of

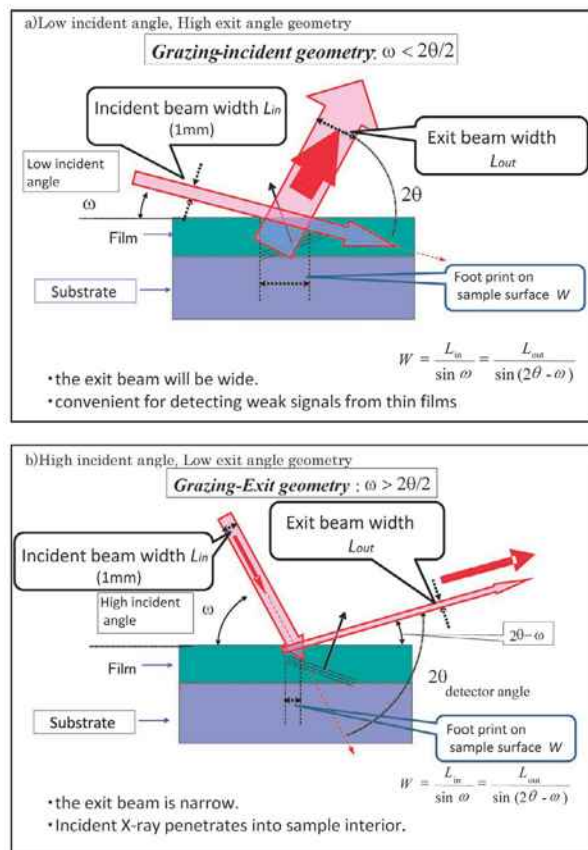


Fig. 5. 2 different geometries of asymmetric reciprocal space map measurement.

- (a) Low angle incident, High angle exit geometry.
 (b) High angle incident, Low angle exit geometry.

diffracted beam should be the same size as a strip of the detecting elements. The geometry shown in Fig. 5(b) should therefore be used for RSM measurements using 1D detector. Even if it is the symmetric-geometry, the width of incident beam should be controlled to be the same width as that of a detecting strip. A wider incident beam causes the reduction of resolution, and it often causes a streak in RSM data running along the trace of 2θ motion (thus, along the Ewald's circle).

• 0-dimensional mode

A 1D detector has many strips on the detection area, but by canceling out the 2θ information (positional sensitivity), this detector can be used as a 0D detector. This mode is called "0D mode" measurement. By using this mode, optical alignment and sample alignment can be carried out like using a scintillation counter. Also, with any kind of receiving optics, various measurements, such as high resolution Rocking Curve measurement (3rd lecture)⁽¹⁰⁾ and X-ray reflectivity (5th lecture)⁽¹¹⁾, will be available. Selection of measuring modes can be performed in a manual control window or in measurement dialog boxes.

2.3. 2D Detector

There have been already equipped 2D detectors such as CCDs, Imaging Plates, X-ray films in a conventional

XRD system, but these detectors or recording media have some disadvantages like sensitivity, reading time, etc.

Recently, solid-state semiconductor devices such as X-ray detectors where detection pixels are arranged in 2 dimensional arrays on a detection area, have come to be commercially available. The SmartLab system can be equipped with “PILATUS 100K/R” as a high speed and quick read-time, single-photon counting 2D detector, which also has high dynamic range and high sensitivity. The details and features of this detector are described in articles^{(3)-(5),(12)}.

In comparison with a 2D gaseous detector, 2D solid-state semiconductor detectors have various advantages, including not only the high energy discrimination, but also the applicability of TDI mode like a 1D detector utilizing its potentiality of short readout time. In addition, due to the difference in finite thickness in the active sensing regions, solid-state semiconductor detectors have advantages (thin sensing region) over the gaseous detectors in the aspect of oblique incidence of X-ray to detectors.

2.3.1. Principle of performing “high-speed measurement”

Figure 6 shows a SmartLab system equipped with PILATUS 100K/R. The incident X-ray and diffracted X-rays are drawn as red lines. 2-dimensionally arranged

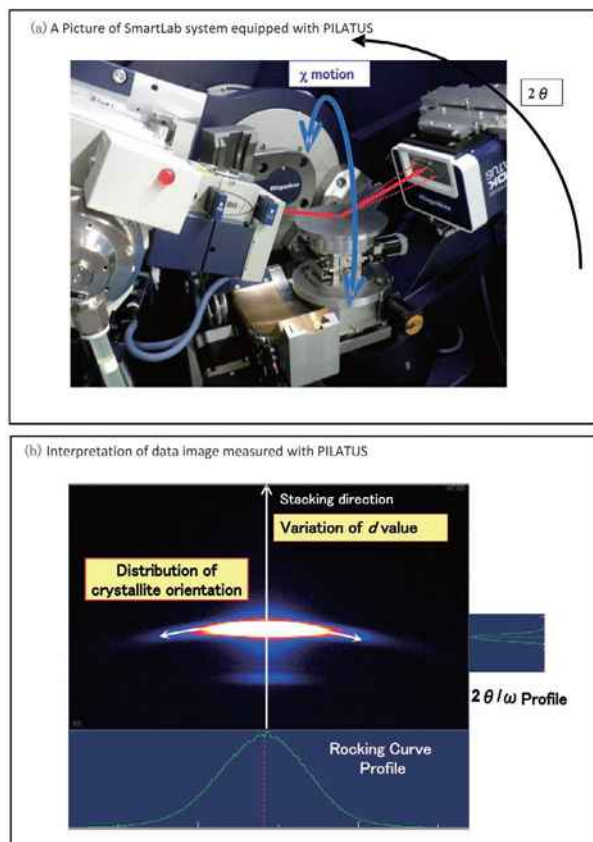


Fig. 6. (a) A picture of SmartLab system equipped with PILATUS 100K/R. (b) Interpretation of data image measured with PILATUS.

detecting pixels can record data which can be obtained by data acquisition with the goniometric motion of 2θ scan and with that of almost equivalent to χ scan. An example of a data image measured by 2D detector is shown in Fig. 6(b). With this figure, it can be easily recognized that information of 2θ (i.e. information of d-spacing, thus those of lattice constants) and distribution of crystallite orientation (mosaic spreading) is recorded in a single shot of 2D image data, then, high speed measurement is attained.

2.3.2. 2D detector for thin film sample measurement

In a previous paragraph, it is explained as “data acquisition with that of almost equivalent to χ scan”. It should be noted that it is, expressly, not equivalent to the data acquisition with χ scan. As shown in Fig. 6(a), the diffracted beam which is detected at the position close to the edge of 2-dimensional detector enters the detector in a condition far away from the normal incidence to the detector surface; i.e., the shape of the diffraction spots would be distorted due to the effect of oblique projection to the detecting plane.

Another factor which should be taken into account for the analysis of data detected close to the edge of 2D detectors is the interpretation of azimuthal directions, which is crucial for the analysis of epitaxial films. If the detection area is large enough, one might surmise that all of the diffraction signals both for $\theta/2\theta$ scans and In-plane scans can be obtained simultaneously, yet this is not correct. The diffraction condition should be satisfied with the sample rotation. This indicates that the diffraction condition should be satisfied with the sample rotation with ϕ axis for the diffraction signals observed with In-plane scans. Thus, a 2D data image with a single snapshot (or Still mode measurement) will collect signals with different azimuth information for the points of center and edge (right and left edge in figure) in the detection area. For the RSM measurements for single crystalline epitaxial films or substrates, RSM measurements of wide χ angle range covered with a big detection area detector are not appropriate. Instead, measurements with small χ steps, followed by the compilation data processing of these data in the data analysis software are effective. One may wonder whether the ω rotation will not be required as for the ϕ rotation of a sample. The answer is that it is required but it can be attained with the TDI mode scan. The PILATUS 100K/R can be covered the wide range of $2\theta/\omega$ angles by using TDI measurement mode like the 1D detector^{(5),(13),(14)}.

Cautions mentioned above are very important in measurements of epitaxial films or single crystalline samples, but almost negligible in those for thin film samples with textures of weak or no preferred orientations.

For the general measurement with 2D detector, nothing can be placed between sample and detector (Fig. 6(a)), so it is difficult to avoid scattering signals except

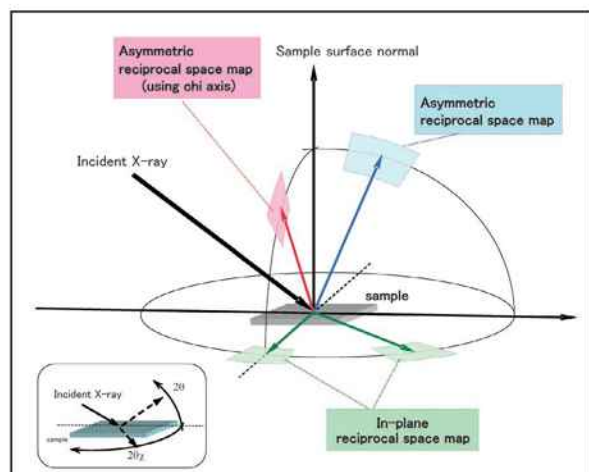


Fig. 7. Geometry of reciprocal space map.

from a sample itself, such as scattering from sample stages, or from dome covers or window materials of high temperature stages, etc.

The 2D detector will also work as a powerful tool of analysis via wide angle RSM measurements for epitaxial films with lattice distortions or tilting. High angular resolution will not be required for RSM measurements for these films, rather, data for the wide area in reciprocal space will be preferable. These requirements for measurements are complementary with the features of 2D detectors with TDI mode.

The geometries of RSM measurements are schematically shown in Fig. 7. The area marked with red lines is that for RSM measured by $2\theta/\omega$ scans combined with χ axis step-tilting (RSM with skew geometry for asymmetric lattice planes), which can be measured with 2D detector. The relative χ angle range will be ± 5 to 10 degrees at one $2\theta/\omega$ scan. Iterative motions of a goniometer as repeating χ steps and $2\theta/\omega$ scans, will lead to obtaining data for a wide area RSM.

As explained in the 6th lecture “Small angle X-ray scattering measurement”⁽¹⁵⁾ and 7th lecture “Pole figure measurement”⁽¹⁶⁾, 2D detectors have great advantages in these measurements, especially for GI-SAXS measurements^{(15),(17)-(19)}.

For the measurement using a 2D detector, it is generally required to set the incident X-ray beam as small as possible to be a point shape. However, this does not necessarily mean that a line-focused X-ray source should be changed to a point-focus source. For example, a combined set of narrow limit slits and PSCs (Parallel Slit Collimator) or collimators can be adopted for this purpose. Additionally, the SmartLab system can be equipped with a unique functional tool “CBO-*f*” as a converter from a line-shaped beam to a point-shaped beam in the incident optics.

Moreover, a line-shaped incident beam itself can be adopted for RSM measurements where higher signal intensities are preferred over the resolution. The data image with this optics configuration will be suffer from defocusing due to the umbrella effect, but the center of

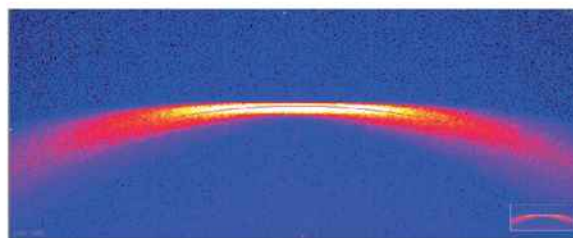


Fig. 8. Hi speed measurement with 2D detector (line focus).

the image will not be affected as much, as shown in Fig. 8.

3. Summary of this lecture course

With this, the eight lectures for basic measurement techniques of X-ray characterization of thin-film samples have been published. Titles for all lectures are listed as below.

- I. “Overview” 2008, Vol. 24, No. 1
- II. “Out-of-plane diffraction measurement” 2008, Vol. 25, No. 1
- III. “High resolution X-ray diffractometry” 2009, Vol. 25, No. 2
- IV. “In-plane XRD measurement” 2010, Vol. 26, No. 1
- V. “X-ray reflectivity measurement” 2010, Vol. 26, No. 2
- VI. “Small angle X-ray scattering” 2011, Vol. 27, No. 1
- VII. “Pole figure measurement” 2011, Vol. 27, No. 2
- VIII. “Detectors and Series Summary” this lecture

Recently, thin film materials are exhibiting remarkable evolution and progress. It may be required soon to make the updating revision for the list of measurement examples (1st lecture, Table 2)⁽¹⁾.

We have been asked many questions about measurement and analytical techniques from many users in the various fields. For the answers to each question, we have come to plan and edit this “X-ray Thin-film Measurement Techniques” lecture course. We hope these lectures will be helpful for many users, and may assist the thin film material research activity in the world.

References

- (1) K. Inaba: *The Rigaku Journal (English version)*, **24** (2008), No. 1, 10–15.
- (2) *The Rigaku Journal (English version)*, **24** (2008), No. 1, 30–32.
- (3) Ch. Broennimann, E. F. Eikenberry, B. Henrich, R. Horisberger, G. Huelsen, E. Pohtl, B. Schmitt, C. Schulze-Briese, M. Suzuki, T. Tomizaki, H. Toyokawa and A. Wagner: *J. Synchrotron Rad.*, **13** (2006), 120–130.
- (4) T. Taguchi, C. Brönnimann and E. F. Eikenberry: *Powder Diffraction*, **23** (2008), 101–105.
- (5) P. Kraft, A. Bergamaschi, Ch. Broennimann, R. Dinapoli, E. F. Eikenberry, B. Henrich, I. Johansson, A. Mozzanica, C. M. Schlepütz, P. R. Willmatt and B. Schmitt: *J. Synchrotron Rad.*, **16** (2009), 368–375.
- (6) T. Mitsunaga: *The Rigaku Journal (English version)*, **25** (2009),

- No. 1, 7–12.
- (7) S. Kobayashi: *The Rigaku Journal (English version)*, **26** (2010), No. 1, 3–11.
- (8) A. Kishi: *The Rigaku Journal (English version)*, **25** (2009), No. 2, 9–13.
- (9) Y. Namatame: *The Rigaku Journal (English version)*, **27** (2011), No. 1, 6–8.
- (10) T. Konya: *The Rigaku Journal (English version)*, **25** (2009), No. 2, 1–8.
- (11) M. Yasaka: *The Rigaku Journal (English version)*, **26** (2010), No. 2, 1–9.
- (12) Y. F. Yano, T. Uruga, H. Tanida, H. Toyokawa, Y. Terada and H. Yamada: *Jour. Synchrotron Rad.*, **17** (2010), 511–516.
- (13) T. Nakajima, T. Tsuchiya and T. Kumagai: *Cryst. Growth Design*, **10** (2010), 4861–4867.
- (14) T. Nakajima, T. Tsuchiya and T. Kumagai: *Cryst. Eng. Comm.*, **13** (2011), 158–166.
- (15) A. Ogi and K. Inaba: *The Rigaku Journal (English version)*, **27** (2011), No. 1, 1–5.
- (16) K. Nagao and E. Kagami: *The Rigaku Journal (English version)*, **27** (2011), No. 2, 6–14.
- (17) Y. Ito: *The Rigaku Journal (English version)*, **25** (2009), No. 1, 1–6.
- (18) Y. Ito, K. Omote, Y. Okazaki, Y. Nakayaka and H. Kawada: *Proc. of SPIE.*, **7638** (2010), 763810-1–763810-10.
- (19) K. Omote, Y. Ito and Y. Okazaki: *Proc. of SPIE.*, **7638** (2010), 763811-1–763811-8.



**X-ray Diffraction Analysis
for Thin Film Samples**

Training Textbook

Table of Contents

| | |
|---|----------|
| Chapter 1 | |
| X-ray Diffractometers and Optics Used in Thin Film Analysis..... | 3 |
| 1.1 X-ray Diffractometers for Thin Film Analysis | 4 |
| 1.2 Goniometer, Sample Stage, and Attenuator | 5 |
| 1.2.1 Goniometer | 5 |
| 1.2.2 Sample Stage..... | 6 |
| 1.2.3 Attenuator..... | 6 |
| 1.3 Types and Features of Optical Devices..... | 7 |
| 1.3.1 Paraboloidal Synthetic Multilayer Mirror..... | 7 |
| 1.3.2 Channel-Cut Crystal..... | 9 |
| 1.3.3 Optics Based on Channel-Cut Crystal | 9 |
| 1.3.4 Width-Limiting Slit | 12 |
| 1.3.5 Height Limiting Slit (Length Limiting Slit)..... | 13 |
| 1.3.6 Soller Slit..... | 14 |
| 1.3.7 Examples of Measurement Techniques Using Soller Slits..... | 15 |



Chapter 1

X-ray Diffractometers and Optics Used in Thin Film Analysis

While the crystallinity of the measured object is relatively restricted in a powder sample or a single crystal sample, a thin film sample may include a range of crystallinity types. For example, in the case of a polycrystalline film and an epitaxial film on a single crystal substrate, the former film will sometimes have low crystallinity and a low preferred orientation, while the latter film has high crystallinity comparable to a thin single crystal. A comparison of the X-ray diffraction profiles of these samples will show large differences in properties, including diffraction peak width, angle difference between two or more peaks, and peak shape. To analyze the thin film samples correctly, we must first acquire correct profiles by selecting the collimation (divergence angle) and monochromaticity of the X-rays according to the crystallinity or other properties of the sample.

Although the purpose of measurement is to observe the preferred orientation or an extremely thin layer, thin film samples can often require observations from two or more directions by thin film or in-plane measurements, in addition to ordinary θ - 2θ measurement. In such cases, we must rotate the sample or the measurement axis to an orientation different from the θ - 2θ scan and measure the angles.

This chapter gives an overview of the X-ray diffractometers used for thin film analysis and describes the optics used to set the resolution and criteria for selecting the resolution of the measurement optics.



1.1 X-ray Diffractometers for Thin Film Analysis

An X-ray diffractometer generally consists of three parts: an X-ray source, a mechanical section (goniometer), and a counter. Since thin film samples vary widely in crystallinity and preferred orientation, we must often measure a sample by tilting it in various directions and changing the scanning direction of the detector. Thus, an X-ray diffractometer for thin film analysis has additional functions in the mechanical section (goniometer) and sample stage section.

When we change the scanning direction of the detector or the direction to measure the diffraction angle 2θ , we must also set the angle resolution accordingly. In other cases, we may need to change the collimation and monochromaticity of the X-ray beam for measurements according to the crystallinity of the sample. In these cases, to change beam characteristics, we must add optical devices to the incident and receiving optics in the front and rear of the sample stage.

Fig. 1.1.1 shows the external appearance of the horizontal sample mount X-ray diffractometers, the SmartLab and TTRAX III. The figure also gives a schematic diagram of the system configuration. (The Ultima III and Ultima IV are X-ray diffractometers that use X-ray generators differing from the TTRAX III. This text refers to the Ultima III, Ultima IV and TTRAX III simply as the Ultima/TTRAX series.)

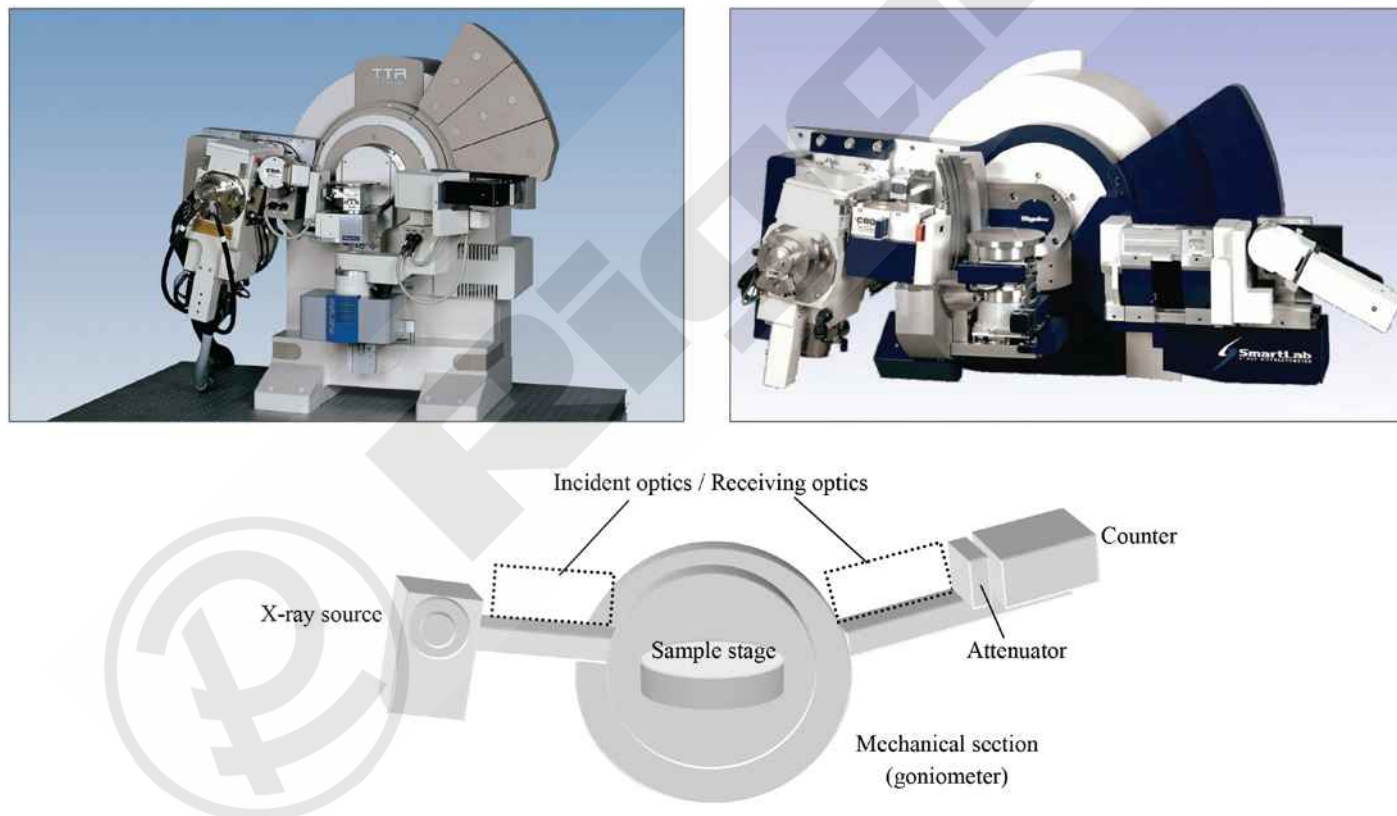


Figure 1.1.1. Configuration of X-ray diffractometer

From above: external appearance of TTRAX III, external appearance of SmartLab (9kW), and schematic diagram of the system configuration

1.2 Goniometer, Sample Stage, and Attenuator

1.2.1 Goniometer

A horizontal sample mount X-ray diffractometer has the two following goniometer axes.

- θ_s axis: The axis for setting the angle of the X-ray source with respect to the sample surface. (The "S" in " θ_s " refers to "source.")
- θ_D axis: The axis for setting the angle of the detector with respect to the sample surface. (The "D" in " θ_D " refers to "detector.")

The θ_s axis and the θ_D axis are used to set 2θ , the diffraction angle.

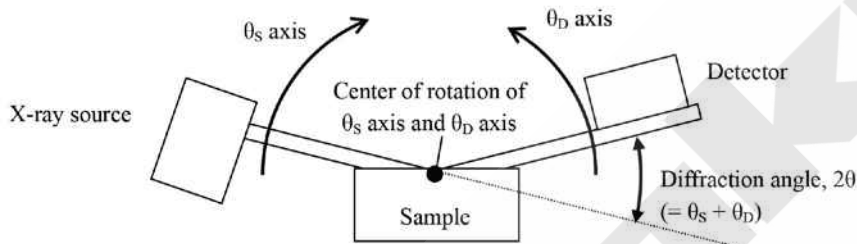


Figure 1.2.1. Goniometer axes in horizontal sample mount X-ray diffractometer

The optional **in-plane arm** has a $2\theta_x$ axis, which rotates the detector in a plane parallel to the sample surface. In in-plane measurements, which perform measurements in the range close to $\theta_s = 0^\circ$ and $\theta_D = 0^\circ$, the diffraction angle 2θ can be assumed to take the same value as the $2\theta_x$ axis. If the measurement range is not close to $\theta_s = 0^\circ$ and $\theta_D = 0^\circ$, as in pole figure measurements or reciprocal space mapping measurements (mesh measurement), diffraction angle 2θ differs from $2\theta_x$ and takes a value calculated based on angles, θ_s , θ_D , and $2\theta_x$.

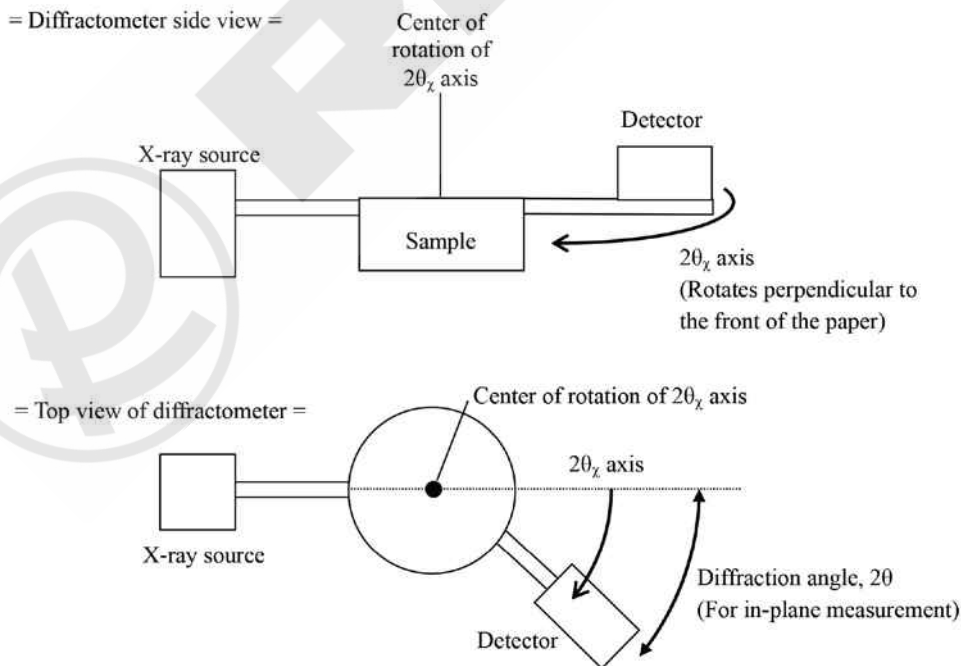


Figure 1.2.2. In-plane axis (optional)

1.2 Goniometer, Sample Stage, and Attenuator

1.2.2 Sample Stage

The measurement sample is mounted on the sample stage at the center of the goniometer. The sample stage has axes for adjusting the angles and positions of the sample based on the purpose of the measurement, including sample rotation, sample swing, and sample translation. Fig. 1.2.3 shows an overview of the axes incorporated into the sample stage. Note that features such as the shape of the sample stage, the number of axes in the sample stage, and the range of motion of each axis vary depending on the model.

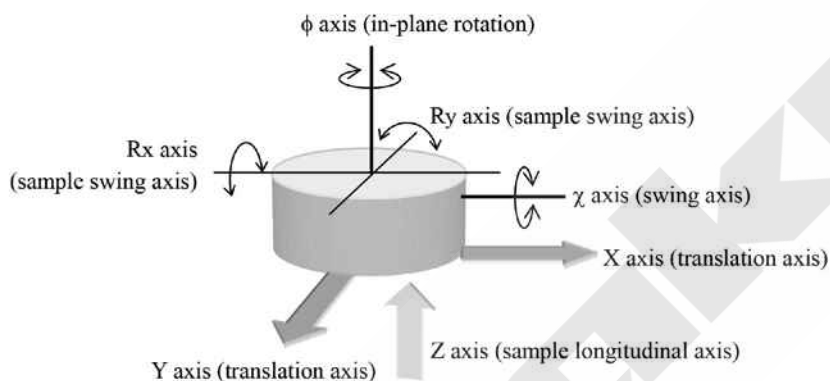


Figure 1.2.3. Sample stage of horizontal sample mount goniometer

1.2.3 Attenuator

For samples with high crystallinity, the diffracted X-ray beam may have extremely high intensity, and the scintillation counter may not be able to count correctly. In general, a scintillation counter can withstand a counting rate of up to approximately 800 thousand cps. To count X-rays with intensities above this value, we must use an **attenuator**.

An attenuator is an Al plate of a specified thickness. The attenuator is placed before the scintillation counter to attenuate X-ray intensities to levels that can be counted by the scintillation counter. The intensity counted with the attenuator inserted is multiplied by the attenuation factor measured in advance for conversion to the direct X-ray intensity that would have been registered without the Al plate.

An automated attenuator incorporates two or more Al plates of differing thicknesses, switching the plates by a rotation mechanism. The plate with the suitable attenuation factor is chosen depending on the X-ray intensity to be measured.

Table 1.2.1. Types of attenuators

| Name | Inside the attenuator |
|----------------------|---|
| Open | None |
| Ni | $K\beta$ filter for Cu lines. A nickel foil whose thickness is adjusted based on the difference in absorption coefficients of Ni for Cu $K\alpha$ and $K\beta$ lines so that the intensity ratio of the Cu $K\alpha$ and $K\beta$ lines is 100:1. |
| 1/X (three types) | An aluminum foil whose thickness is adjusted so that the attenuation factor for the Cu $K\alpha$ line is approximately 1/X. (The value of X varies, depending on the diffractometer.) |

SmartLab offers an automated attenuator mode and switches attenuators automatically when it detects large intensity variations during measurement. The Ultima/TTRAX series provides functions for specifying the angular positions to switch attenuators and perform measurements while changing the attenuators one after another. Combined with attenuators, the scintillation counter can make correct counts of intensity variations across approximately nine orders of magnitude.

1.3 Types and Features of Optical Devices

Optical devices to be used for SmartLab and the Ultima/TTRAX series are listed below. These optical devices are combined and inserted in the incident and receiving optics and adjusted to provide the optical resolution based on the purpose. This section describes the components and features of these optical devices.

- Paraboloidal synthetic multilayer mirror
 - CBO unit
- Channel-cut crystals
 - Double-crystal monochromator
 - Four-crystal monochromator
 - Double-crystal analyzer
- Width-limiting slit
 - Incident slit
 - Receiving slit
- Height-limiting slit
- Soller slit

1.3.1 Paraboloidal Synthetic Multilayer Mirror

A **paraboloidal synthetic multilayer mirror** efficiently monochromatizes and collimates the divergent beam generated from the X-ray source.

On a substrate with a flat surface, alternate layers of heavy and light elements (W film and B₄C film or Si film) are stacked periodically by the sputtering technique. This structure creates regular variations in electron density and generates diffraction phenomena like a crystal. To generate the diffraction phenomena selectively in the characteristic X-rays used in the X-ray diffraction measurement and to extract the X-rays as a collimated beam, the mirror incorporates the following features.

- Each layer of the multilayer film is formed in a paraboloidal curve. When the focus of the X-ray tube is placed at the focus of the paraboloid, the diffracted X-rays form a collimated beam, like waves reflected from a parabolic antenna.
- The thickness of each layer of the multilayer film is designed so that the wavelength of the characteristic X-rays satisfies the diffraction condition. The layers do not have constant thicknesses; they are thinner in the region nearer the focus of the paraboloid and thicker in the region farther from the focus.

1.3 Types and Features of Optical Devices

As a result, the divergent X-rays generated from the X-ray source are collimated and monochromatized with wavelength components around the Cu K α line. The monochromaticity in terms of the intensity ratio of the Cu K α line to the K β line improves from the original 100:25 to 1000:1. The collimation improves with the divergence angle suppressed to approximately 0.04°.

The shape and thickness of the multilayer film are optimized for each of the wavelengths of the characteristic X-rays used. Thus, when we change the type of the target, we must also change the multilayer mirror.

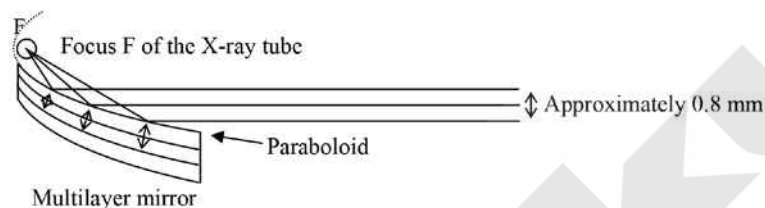


Figure 1.3.1. Paraboloidal synthetic multilayer mirror

In the SmartLab and the Ultima/TTRAX series, the multilayer mirror is stored in the CBO unit.

The **CBO unit** (abbreviation for cross-beam optics) is a mechanism for conveniently switching between the parafocusing method used mainly to measure powder samples and the parallel beam method used to measure thin-film samples. Fig. 1.3.2 shows the structure of the CBO unit.

Although the divergent X-rays generated from the X-ray tube are partially reflected and collimated at the multilayer mirror, certain components do not strike the mirror, propagating instead with divergent characteristics unaltered. These two components propagate at different heights. By using a slit with an appropriate gap height (**selection slit**), we can selectively extract either of these components.

The parafocusing method uses the divergent beam generated from the X-ray tube as the incident X-ray beam as-is. The selection slit used is the “BB” (abbreviation for Bragg-Brentano parafocusing method) slit with a gap at a higher position. The parallel beam method uses the beam collimated on the multilayer mirror as the incident X-ray beam. The selection slit used is the “PB” (the abbreviation for Parallel Beam) slit with a gap at a lower position.

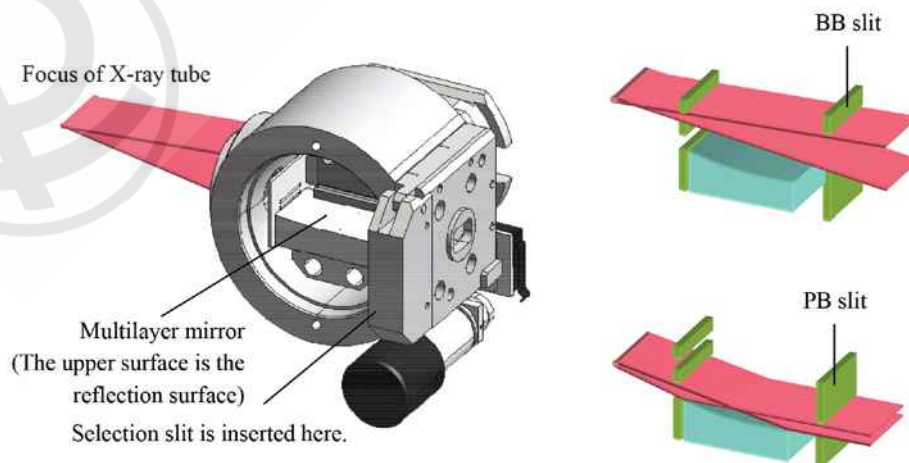


Figure 1.3.2. CBO unit and structure of selection slit

1.3.2 Channel-Cut Crystal

A **channel-cut crystal** is an optical device that uses the diffraction phenomenon generated by a single crystal to monochromatize and collimate X-rays.

The channel-cut crystal used in the SmartLab and the Ultima/TTRAX series is a Ge single crystal block in which a channel is cut, with a structure consisting of two facing single crystals (Fig. 1.3.3). We use a Ge single crystal for its high crystallinity – Ge is sometimes referred to as a perfect crystal (only two types of single-element materials are referred to as perfect crystals: Si and Ge) – and for its atomic scattering factor, which is higher than that of Si.

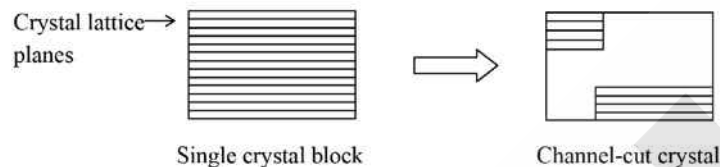


Figure 1.3.3. Channel-cut crystal

Fig. 1.3.4 shows a schematic diagram of an X-ray beam incident on a channel-cut crystal. Among the X-rays incident on the channel-cut crystal, those incident at the diffraction angle θ_B satisfying the Bragg formula are diffracted and output from the outlet of the channel-cut crystal. Since the crystallinity of the Ge single crystal is extremely high and significantly restricts diffraction, the X-ray beam is highly collimated and monochromatized after passing through the channel-cut crystal.

The crystal structure reflects the X-rays twice, not once, to extract the X-ray beam parallel to the incident X-ray beam and simplify equipment design.

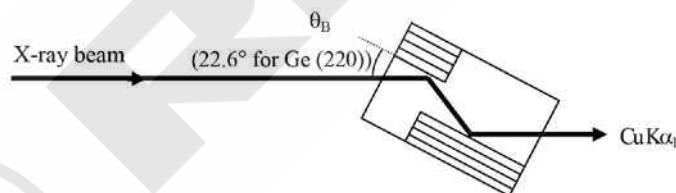


Figure 1.3.4. Monochromatization and collimation of X-rays by Ge (220) channel-cut crystal

1.3.3 Optics Based on Channel-Cut Crystal

The incident and receiving optics based on a channel-cut crystal include those listed below.

- Incident optics – monochromator
 - Ge (220) double-crystal monochromator
 - Ge (220) four-crystal monochromator (SmartLab only)
 - Ge (400) double-crystal monochromator (SmartLab only)
- Receiving optics – analyzer
 - Ge (220) two-bounce analyzer (SmartLab only)
 - Ge (400) two-bounce analyzer (SmartLab only)

1.3 Types and Features of Optical Devices

A. Monochromator

A channel-cut crystal used in the incident optics is called a **monochromator**. Inserted next to the CBO unit, a monochromator provides higher collimation and monochromaticity than a paraboloidal synthetic multilayer mirror. Channel-cut crystal monochromators are classified by the number of reflections and surface indices of the channel-cut crystal. Select a suitable model based on the crystallinity of the sample and the purpose of the measurement.

A **double-crystal monochromator** uses one channel-cut crystal (two reflections). A **four-crystal monochromator** combines two channel-cut crystals (four reflections), as shown in Fig. 1.3.5.

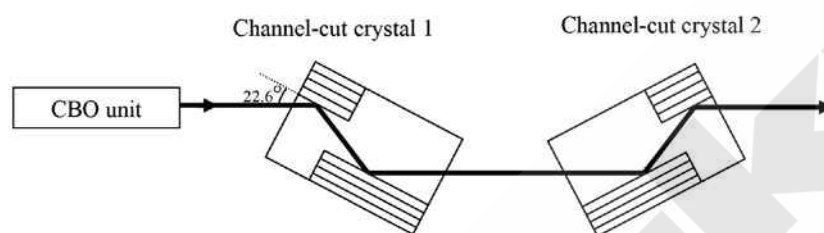


Figure 1.3.5. Ge (220) four-crystal monochromator

The double-crystal monochromator and the four-crystal monochromator differ in the aspects listed below.

- **Monochromaticity**

The double-crystal monochromator can selectively extract only the Cu $K\alpha_1$ line. The four-crystal monochromator can provide higher monochromaticity than the double-crystal monochromator and extracts only part of the Cu $K\alpha_1$ line.

- **Angular resolution**

While the angular resolution (apparent X-ray divergence angle) of the X-rays output from the double-crystal monochromator depends on the diffraction angle of the measurement sample, the angular resolution of the X-rays output from the four-crystal monochromator is constant across a wide diffraction angle range. Fig. 1.3.6 shows the diffraction angle dependence of the angular resolution for each monochromator.

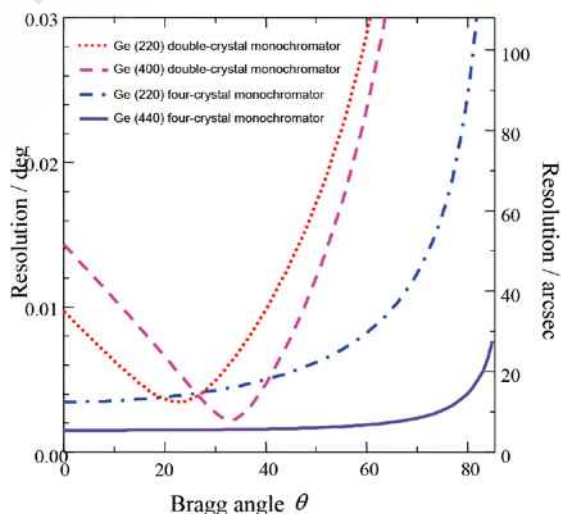


Figure 1.3.6. Monochromators and their resolution

- **Diffraction intensity**

Since the four-crystal monochromator selects X-rays that more rigorously satisfy the diffraction condition, it results in lower X-ray intensity than the double-crystal monochromator.

Due to the preceding characteristics, select a double-crystal monochromator or four-crystal monochromator after considering both resolution and intensity. If the material and crystal lattice plane of the measured object are known, a suitable double-crystal monochromator can give both high resolution and high intensity, producing a profile rapidly. If the Bragg angle to be measured is in a low-resolution range with the double-crystal monochromator or if you need to measure various materials or two or more crystal lattice planes of the same material sequentially, select the more versatile four-crystal monochromator.

The **diffraction plane indices of the double-crystal monochromator** (Ge (220) and Ge (400)) differ in the aspects listed below.

- **Diffraction angle dependence of angular resolution**

As shown in Fig. 1.3.6, the double-crystal monochromator outputs X-rays with the angular divergence reaching the minimum (and thus the angular resolution in a diffraction measurement reaching the maximum) when the Bragg angle of the channel-cut crystal agrees with the Bragg angle of the measurement sample. The Bragg angle is $\theta_B = 22.6^\circ$ for Ge (220) and $\theta_B = 33.0^\circ$ for Ge (440).

- **Diffraction intensity**

The intensity of the X-rays output from a channel-cut crystal depends on the crystal structure factor of the crystal lattice planes used in the channel-cut crystal. The crystal structure factor corresponding to the Cu $K\alpha$ line is 181.8 for Ge (220) and 155.1 for Ge (400). That is, when X-rays of the same intensity enter the crystal, X-rays diffracted on the Ge (220) crystal lattice planes have a greater intensity than those diffracted on the Ge (400) crystal lattice planes.

Given the preceding characteristics, select the Ge diffraction plane of the double-crystal monochromator based on the following criteria.

If the material and the crystal lattice plane of the measured object are known, it helps to use a monochromator with indices suitable for the diffraction angle. Since the diffraction angle of the Ge (400) monochromator ($\theta_B =$ approximately 33°) is close to the diffraction angles of GaAs (400) ($\theta_B =$ approximately 33.0°) and Si (400) ($\theta_B =$ approximately 34.5°), which are often used as substrates of thin film samples, this can be a powerful tool when evaluating epitaxial films deposited on these substrates.

Similarly, when measuring a material with a diffraction angle close to that of Ge (220) ($\theta_B =$ approximately 22.6°), the Ge (220) double-crystal monochromator can be useful. If we use a double-crystal monochromator simply to monochromatize the beam to the Cu $K\alpha_1$ line, the Ge (220) double-crystal monochromator is more effective, since it has a higher crystal structure factor and provides higher intensity.

The diffraction plane indices of the **four-crystal monochromator** (Ge (220) and Ge (440)) differ in the aspects listed below.

- **Angular resolution**

A four-crystal monochromator provides high resolution across a wide diffraction angle range. Here, a channel-cut crystal with higher reflection indices provides higher monochromaticity and collimation.

1.3 Types and Features of Optical Devices

- **Diffraction intensity**

Since the crystal structure factor of the Ge (440) plane is 121.3 and lower than the value (181.8) for the Ge (220) plane, the usable X-ray intensity is lower for the Ge (440) plane.

Given the preceding characteristics, select the Ge (440) four-crystal monochromator when measuring a single crystal substrate of a material with extremely high crystallinity (e.g., Si, GaAs, or quartz). If we use the Ge (440) four-crystal monochromator for a material with relatively low crystallinity, the measurement will be time-consuming, since the diffracted X-ray intensity from the sample is relatively low.

B. Analyzer crystal

A channel-cut crystal used in the receiving optics is called an **analyzer**. An analyzer restricts both the 2θ take-off angle and wavelength, allowing precise observations of the diffraction angle. The 2θ angle receiving width of the Ge (220) analyzer crystal is approximately 0.003° .

When we use an analyzer crystal, we must also use receiving slits of the same width as the incident slit before and after the analyzer crystal to shield the scattered beam (analyzer streak) by multiple scattering (refer to Chapter 5) in the analyzer crystal.

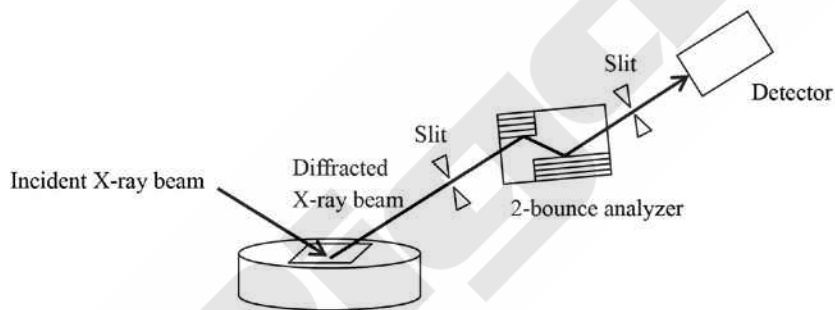


Figure 1.3.7. Two-bounce analyzer

1.3.4 Width-Limiting Slit

A **width-limiting slit** restricts the size of the X-ray beam vertically. It can be controlled from the PC and is used in both incident and receiving optics.

A. Incident slit

(IS in SmartLab and Divergence Slit (DS) in the Ultima/TTRAX series)

The width-limiting slit used in the incident optics restricts the width of the sample area irradiated by X-rays. In X-ray diffraction measurements, the change in area irradiated by X-rays must be suppressed during measurement, so that a sufficiently narrow slit is used to restrict the X-rays within the area of the sample, or conversely, a sufficiently wide slit is used to soak the sample in the X-rays (complete soaking). In contrast, with X-ray reflectivity measurements, a narrow slit is always used, since the area of X-ray irradiation in the sample area must be restricted. Fig. 1.3.9 shows the relationship between the width of the incident slit, the X-ray incident angle, and the width of the sample area irradiated by X-rays.

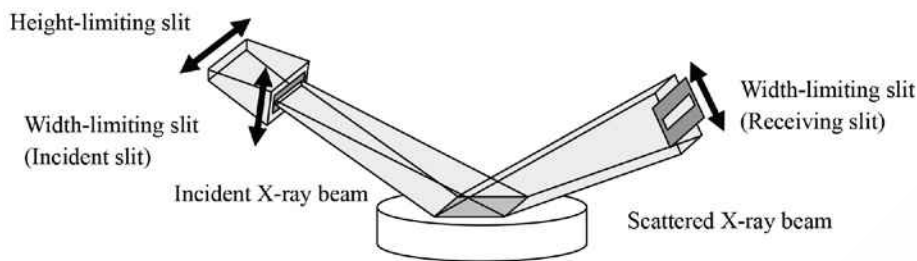


Figure 1.3.8. Insertion direction of width-limiting slit and height-limiting slit

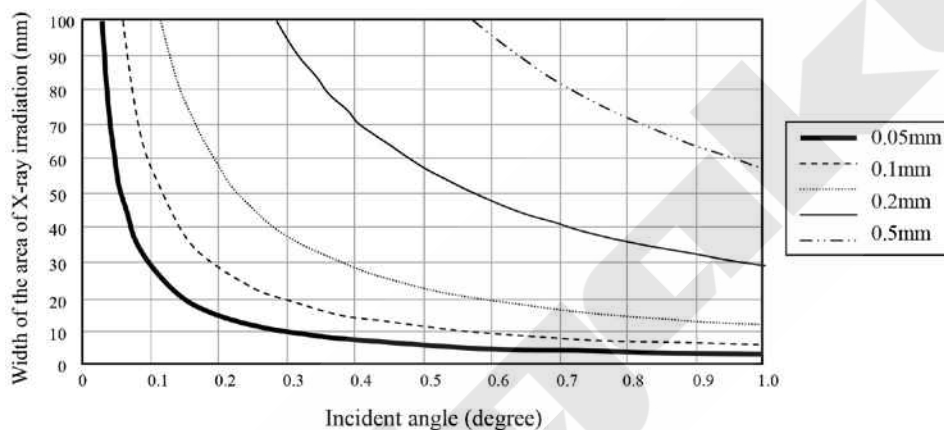


Figure 1.3.9. Width of the area of X-ray irradiation determined by the incident slit

B. Receiving slit

(RS1 and RS2 in SmartLab and Scattering Slit (SS) and Receiving Slit (RS) in the Ultima/TTRAX series)

The receiving slits are used to determine the 2θ resolution or to shield the scattered X-rays. In the symmetric $2\theta/\omega$ measurement, in which the incident X-ray beam and the diffracted X-ray beam have the same width, the receiving slits are set to the same width as the incident slit to avoid blocking the diffracted X-rays. In thin film measurements (2θ scan) or asymmetric $2\theta/\omega$ measurements in which incident X-rays and diffracted X-rays have different widths or in in-plane measurements in which vertical angular resolution can be disregarded, measurements are performed with receiving slits set to widths different from the DS or with a completely open receiving slit combined with the Soller slit (described further below).

1.3.5 Height Limiting Slit (Length Limiting Slit)

The **height limiting slit** (the **length limiting slit** in SmartLab) restricts the width of the area of X-ray irradiation in the longitudinal direction.

The height limiting slit is used to determine the area irradiated by X-rays combined with the incident slit. Note that the paraboloidal synthetic multilayer mirror in the CBO unit collimates X-rays only vertically and that X-rays are permitted to disperse widely in the lengthwise longitudinal direction of the equipment. Thus, at the sample position, the X-ray beam spreads beyond the width set by the height limiting slit. When a thin-film sample is measured, the sample is also often rotated in-plane. For these reasons, we must select the slits after considering the width of the sample both laterally and longitudinally.

1.3 Types and Features of Optical Devices



Figure 1.3.10. Height limiting slit; left: SmartLab; right: Ultima/TTRAX series

1.3.6 Soller Slit

A **Soller slit** is a set of metal foils placed at constant intervals. It extracts only those X-rays parallel to the gaps between the metal foils, suppressing the divergence of the X-ray beam.

The divergence angle of the X-ray beam is smaller when the interval of the metal foils is smaller and the length of the Soller slit is longer. Fig. 1.3.11 shows a schematic diagram of the vertical Soller slit. The direction of collimation depends on the direction of the metal foils. Horizontally-placed foils suppress vertical divergence of X-rays (**vertical Soller slit**), while vertically-placed foils suppress horizontal divergence of X-rays (**horizontal Soller slit**). Angular resolution depends on the intervals at which metal foils are placed and the length of the Soller slit, ranging between several degrees to several tenth of a degree.



Figure 1.3.11. Vertical Soller slit (Schematic diagram)

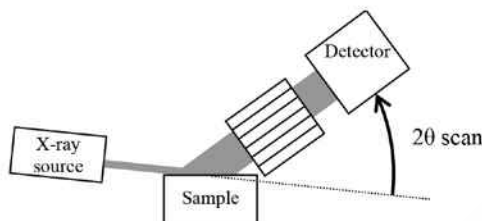
An advantage of a Soller slit is that it does not unnecessarily block wide X-ray beams while providing specific levels of angular resolution.

In measurements with a small X-ray incident angle with respect to the surface such as thin film measurements (2θ scan), asymmetric $2\theta/\omega$ measurements, and in-plane measurements, the irradiated area spreads widely, as does the width of the diffracted X-ray beam. If an ordinary slit is used to capture such X-ray beams, only part of the wide-diffracted beam will pass through the slit, resulting in loss of intensity. In contrast, a Soller slit has a large area through which X-rays can pass, allowing selection of only the X-rays incident in a specific range without blocking the widely spread X-ray beam.

The Soller slit for the receiving optics is designed so that a single Soller slit can be inserted vertically or horizontally. The user can set the slit by selecting the direction in which resolution is required. Two Soller slits can also be inserted side by side to set angular resolution simultaneously in the vertical and horizontal directions. This technique is used for in-plane pole figure measurements in which all possible out-of-plane and in-plane orientations take place.

Fig. 1.3.12 shows a schematic diagram of thin film and in-plane measurements in which the Soller slit is useful.

- Thin film measurement (Side view)
A vertical Soller slit is used.



- In-plane measurement (Top view)
A horizontal Soller slit is used.

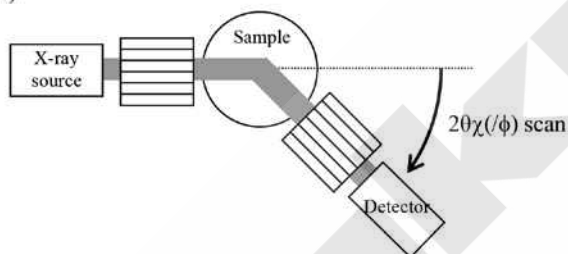


Figure 1.3.12. Examples of measurement techniques using Soller slits

1.3.7 Examples of Measurement Techniques Using Soller Slits

In practical measurements, two or more optical devices are combined for measurement. Here, although higher resolution provides higher measurement precision, it reduces the intensity of the incident and diffracted X-ray beams and prolongs measurements. For efficient evaluations, we must select the optics based on the type of measurement intended and the sample condition. The selection criteria for the optics for each measurement technique are described in the measurement exercises and in the chapters on each of the measurement techniques.

Summary

Divergence angle of incident X-ray beam

| Name | Function | Monochromaticity, $\Delta\lambda/\lambda$ | Divergence angle, $\Delta\theta$ |
|----------------------------|--|---|--|
| Multilayer mirror | Suppression of divergence angle | Cu K α /K β intensity ratio from 100:25 to 1000:1 | 0.04° |
| Channel-cut monochromator | Suppression of divergence angle Improvement in monochromaticity | 3.8×10^{-4} | 0.083° (Near $\theta = 0^\circ$) |
| Four-crystal monochromator | Suppression of divergence angle Improvement in monochromaticity | Ge (220) four-crystal: 1.5×10^{-4} Ge(440) four-crystal: 2.3×10^{-5} | Ge (220) four-crystal: 0.0034° Ge (440) four-crystal: 0.0015° |

1.3 Types and Features of Optical Devices

Receiving angle resolution

| Name | Function | Slit width (DS, SS, RS) | 2θ resolution, $\Delta 2\theta$ |
|------------------|---|---|--|
| Slit | Improvement in 2θ resolution | Open 2 mm 1 mm 0.5 mm 0.2 mm 0.1 mm 0.05 mm | 0.84° 0.34° 0.17° 0.084° 0.034° 0.017° 0.0084° |
| Analyzer crystal | Improvement in 2θ resolution | | 0.003° |
| Soller slit | Improvement in 2θ or $2\theta_x$ resolution (Depends on direction of insertion) | | (Often used for thin-film samples) 1° 0.4° 0.1° |

Trace heavy element analysis for wastewater and river water by X-ray fluorescence spectrometry

—Examples for ppm to sub ppm level analysis of heavy elements—

Takao Moriyama*

1. Introduction

There has been a growing demand globally for the analysis of environmental hazardous substances. In Japan, The Japanese environmental regulation for a trace of zinc in wastewater has been recently revised from 5 mg/l (5 ppm) down to 2 mg/l (2 ppm).

This report introduces an X-ray fluorescence (XRF) analysis for the detection of ppb level of a trace of zinc in wastewater and also hazardous heavy elements in river water using a high sensitivity micro-droplet filter paper, “Ultracarry”[†], and the newly developed vacuum dryer, “Ultradry”.

2. Sample preparation

A liquid sample of wastewater or river water is dropped onto an Ultracarry filter paper, and the maximum dropping amount per specimen on an Ultracarry is 500 μl (see Fig. 1).

If a solution dropped on an Ultracarry is dried by a regular dryer, it normally may take about two hours. In order to shorten the drying time, an Ultradry, which dries the solution by decompression and heating, was employed (see Fig. 2).

The Ultradry can dry a batch of Ultracarry pads and Microcarry filters. Microcarry is a filter paper for the micro-droplet method. The drying time for a batch of filters in the Ultradry is about 20 to 30 minutes. Several samples can be prepared together at the same time. The



Fig. 1. Ultracarry and a dropped solution with a micro pipette.



Fig. 2. Vacuum dryer Ultradry.

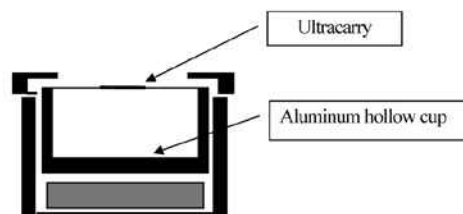


Fig. 3. Schematic diagram of setting an Ultracarry in a sample holder for a tube-above type spectrometer.

dried Ultracarry pads were mounted on aluminum or titanium cups to avoid scattered X-rays. The cups were set in the sample holders of the XRF instrument. (see Fig. 3).

3. XRF Analyses

3.1. Detection of a trace amount of zinc in wastewater

A Rigaku wavelength-dispersive X-ray fluorescence spectrometer ZSX Primus II was used. The spectrometer system has a high spectral resolution that enables a high precision analysis of wastewater with a complex sample matrix.

The solutions with 1, 2, 5, and 10-ppm zinc were prepared by diluting the standard solution used for atomic absorption spectrometry. 500 μl of the solutions were dropped onto Ultracarry pads and then dried with an Ultradry. The XRF spectra for the samples are shown in Fig. 4. The Zn-Kα peak is clearly detectable in the XRF spectrum for the sample with 2-ppm zinc, which is

* Application Laboratory-XRF, Rigaku Corporation.

† U. S. patent No. 7,016,463, EPC Patent No.1650559, Korean patent No. 0713742, Russian patent No. 12005110658, and Taiwanese patent No. I300477.

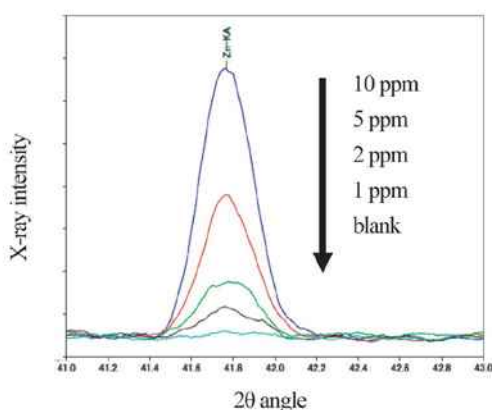


Fig. 4. Ka XRF peaks for Zinc in wastewater (LiF (200) analyzing crystal, 50 kV and 50 mA).

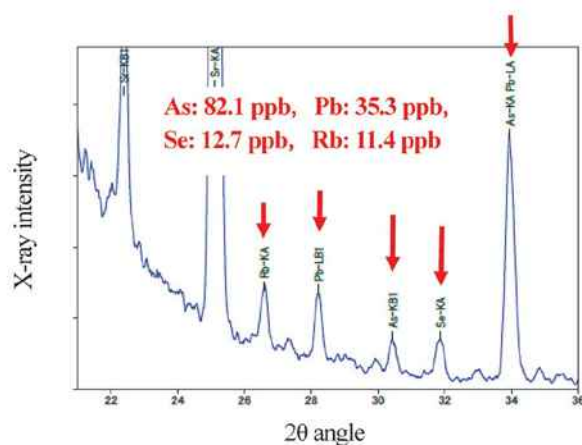


Fig. 5. XRF spectrum of river water (21°–36°2q, LiF (200) analyzing crystal, Cu primary-beam filter, 50 kV and 50 mA).

the criterion of the Japanese environmental regulation for wastewater. The results plotted in Fig. 4 show that the combination of ZSX Primus II and Ultracarry enables wastewater analysis of a trace of zinc down to 1 ppm. The time for drying the Ultracarry was about 30 minutes, and the time for the XRF qualitative analysis per sample was 2 to 3 minutes. A quantitative XRF analysis of a trace amount of zinc in wastewater is also possible by using a calibration curve.

3.2. Detection of trace amounts of heavy elements in river water

The environmental regulation for hazardous heavy elements in river water is in the 10 ppb levels. It is, therefore, necessary to use condensed sample solutions. The Ultradry can be used for this type of analysis because it is equipped with a decompression evaporating apparatus.

A NIST1643c standard (reference solution of river

water) was used in this study. The NIST standard material was first condensed by 50 times with an Ultradry, and then dropped onto an Ultracarry and dried. The XRF spectrum charts of the reference solution are plotted in Figs. 5, 6 and 7. XRF peaks for As (82.1 ppb), Pb (35.3 ppb), Se (12.7 ppb), Rb (11.4 ppb), Zn (73.9 ppb), Cr (19.0 ppb) and V (31.4 ppb) contained in the reference solution are clearly detectable.

4. Conclusions

Our technique of using an Ultracarry filter paper and an Ultradry vacuum dryer shows that the XRF method can be used effectively for a sub ppm level analysis of environmental heavy hazardous elements in wastewater and river water owing to its simple and rapid sample preparation. Since industrial wastewater is likely containing a number of heavy elements, it is therefore useful to perform a prescreening analysis before a normal atomic absorption spectrometer or an inductively coupled plasma spectrometer analysis.

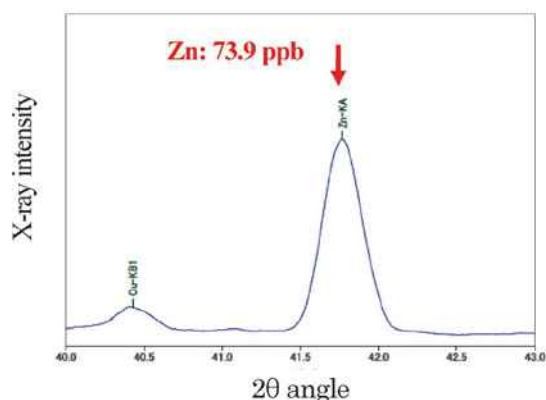


Fig. 6. XRF spectrum of river water (40°–43°2q, LiF (200) analyzing crystal, 50 kV and 50 mA).

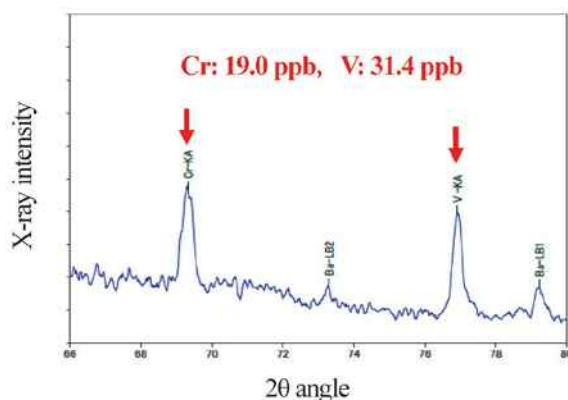


Fig. 7. XRF spectrum of river water (66°–80°2q, LiF (200) analyzing crystal, 50 kV and 50 mA, and the Cr-Kα peak is overlapped by the V-Kβ1 peak).